ABSTRACT

Title of Dissertation:	ELECTROCHEM-MECHANICS CHARACTERIZATION OF SI ELECTRODE/SI BASED SOLID-STATE BATTERY
	Haotian Wang, Doctor of Philosophy, 2022
Dissertation directed by:	Prof. Gary.W.Rubloff Department of Materials Science and Engineering

Li-ion battery (LIB) is a popular energy storage device that predominates the market of microelectronics due to its high energy density and light weight. In the recent trend of electrification of vehicles, LIBs also showed promise in the application of electric vehicles but the energy density of current LIBs with graphite electrode doesn't suffice the need of long driving range. Replacing graphite electrode with alloying type electrodes that have almost ten times higher energy density is thus a necessary route to improve the energy density of LIBs. However, alloying type electrodes, such as Si and Sn, typical undergo enormous volume change (up to 310%) during Li insertion and extraction, which lead to various mechanical problems such as cracking, delamination, and pulverization. These mechanical issues eventually cause catastrophic capacity fading in LIBs and thus, are central topics for the application of alloying type electrodes in next generation LIBs.

This dissertation presents a three-phase experimental study of stress development in Si electrodes and Si based solid state batteries. In the first phase, ex-situ stress characterization in single-c Si electrode was performed to validate Raman spectroscopy as a promising stress characterization technique for Si electrode. In the second phase, in-situ stress characterization in patterned poly-c Si electrode with confocal micro-Raman setup was performed, to investigate the correlation between complex geometries and stress distribution in crystalline Si electrode and the critical size effect. In the last phase, a solid-state battery (SSB) platform device with lateral layout was proposed and validated for stress characterization in Si based SSBs. The platform device can also serve as a versatile testbed for electrochemistry study of bulk SSB components and interfaces. Overall, this dissertation demonstrates a methodology that combines Raman spectroscopy, novel design of electrochemical devices, and computational modeling as a powerful tool for electrochemo-mechanics study of alloying type electrodes and SSB systems.

ELECTROCHEM-MECHANICS CHARACTERIZATION OF SI ELECTRODE/SI BASED SOLID-STATE BATTERY

by

Haotian Wang

Dissertation submitted to the Faculty of the Graduate School of the
University of Maryland, College Park, in partial fulfillment
of the requirements for the degree of
Doctor of Philosophy
2022

Advisory Committee:

Professor Gary.W. Rubloff, Chair
Professor Aris Christou
Associate Professor Sangbok Lee
Assistant Professor Paul Albertus
Assistant Research Scientist David Stewart

Dedication

This dissertation is dedicated to my family and those who helped me in my PhD career

Acknowledgements

First and foremost, I would like to sincerely thank my advisor, Professor Gary Rubloff, for the constant support throughout my PhD career. Your mentorship and enthusiasm about science constantly inspire me to explore and conquer challenging research problems. It has been a pure privilege to work in your group, as I have been exposed to tremendous opportunities to use different resources and collaborate with many great researchers. Then, I would like to thank all members from Rubloff group, for forming a vibrant research community. In particular, I would like to thank Chuan-Fu, David, Nam, and Victoria, for helping me develop ideas for various projects and encouraging my research endeavors. The gratitude extends to Keith, Alex, Angelique, Zoey, Yueming, Sam, and Paolo, thank you for sharing me with your wisdom and your aids on experiments.

There are many other people to thank from groups of Dr.SangBok Lee, Dr.Paul Albertus, Dr.Feng Wang at Brookhaven national lab, and Dr.Yue Qi at Brown University. In particular, Dr.Sangbok Lee and Dr.Paul Albertus have acted as my secondary mentors at University of Maryland, providing valuable insights on my work and constantly sharing resources to help me conquer this multi-disciplinary research work.

I would also like to express special appreciations to Nolan, Don, and Sabrina, for helping me design and fabricate novel testing devices, and broaden the scope of my research interests.

Lastly, I would like to thank my families for their unconditional support in all of my research endeavors.

Table of Contents

List of Figures

List of Abbreviations

1. ESD – Energy storage device
2. LIB – Li-ion battery
3. SSB – Solid state battery
4. FEM – Finite element modeling
5. ECM – Electrochemo-mechanics
6. Redox – Reduction and oxidation
7. PDE – Partial differential equation
8. ALD – Atomic layer deposition
9. TMA – Trimethyl-aluminum
10. LPCVD – Low pressure chemical vapor deposition
11. RIE – Reactive ion etching
12. ICP – Inductively coupled plasma
13. SS – Stainless steel
14. HDPE – High density polyethylene
15. PC – Propylene carbonate
16. DMC – Dimethyl Carbonate
17. GCD – Galvanostatic charge/discharge
18. CV – Cyclic voltammetry
19. EIS – Electrochemical impedance spectroscopy
20. SEM – Scanning electron microscopy
21. EDS – Energy dispersive spectroscopy
22. EBSD – Electron backscattered diffraction
23. XPS – X-ray photoelectron spectroscopy
24. FWHM – Full width half-maximum
25. XRD – X-ray diffraction
26. OCV – Open circuit potential
27. CV – Cylic voltammetry
28. EIS – Electrochemical impedance spectroscopy
29. CEI – Cathode electrolyte interface

Chapter 1: Introduction

With ever-increasing consumption of fossil fuels in the globe, the substantial increase of carbon dioxide emission has led to global warming and extreme weather. The occasional fossil fuel spills also have disastrous impact on the local ecological system and take a high cost for cleanup. Thus, relying on fossil fuels for energy production is an unsustainable route for the future. Renewable energy sources, however, also suffer from limitations: Solar and tidal energy can only be obtained when sunlight and tide are available, while wind and hydro energy can only be accessed at appropriate geologic locations. Therefore, the nature of intermittency and sparsity of renewable energy sources drive the vital need for a reliable form of energy storage.

Currently, electrical energy can be stored in different forms using energy storage devices (ESD) such as capacitors, super magnets, flywheels, and batteries [1]. Among them, battery is one of the most popular ESD and in particular, Li-ion batteries (LIBs) have received increasing attention in the last decade due to its high energy density and light weight [2]. LIBs have been applied to a wide spectrum of electronic systems, from microelectronics to electric vehicles, and are the key to decarbonize the transportation sector. In 2021, about 28% of total U.S. energy consumption was used for transportation, with more than 90% of the energy consumed in the form of

petroleum[3]. Therefore, replacement of fossil fuels with batteries in vehicles will greatly increase the pace of carbon neutralization.

Although a remarkable progress of electrification in the transportation sector has been witnessed in the past decade, battery is still the bottleneck in electric vehicles, as energy density of current LIBs is much lower than fossil fuels and the charging speed of LIBs is typically much slower than filling a gas tank. To improve the energy and power density of LIBs, novel battery architectures coupled with high energy density electrodes need to be developed. Recently, various 3D structures with improved surface area to volume ratio have been proposed[4,5], but employment of high energy density electrodes in these systems is still facing challenges: High energy density electrodes, such as Si and Sn, undergo large volume change during Li insertion and extraction, which leads to mechanical failure of electrodes and rapid capacity fading in Li-ion batteries[6]. The mechanical issues can be more severe in 3D architectures as sharp corners potentially cause stress concentration and accelerate the mechanical degradation of electrodes. Therefore, understanding the stress development in high energy density electrodes and stress distribution induced by complex geometries are critical for the development of next generation high energy density LIBs.

This dissertation presents experimental studies of stress characterization in Si electrodes and Si based solid-state batteries. In this dissertation, Si electrodes in the

bulk form and model devices using Si thin films are both investigated. By integrating experimental results with finite element modeling (FEM), the electrochemo-mechanical (ECM) coupled effect in Si electrodes and heterogeneity problems involved with complex geometries are addressed. Overall, this dissertation represents a novel application of semiconductor technologies in the study of electrochemical devices. We hope that the methodology and understanding obtained from this dissertation would pave an intriguing path for future ECM studies and development of next generation LIBs.

The following sections provide an overview of the basic principles of Li-ion batteries, mechanical challenges of Si electrodes, Raman spectroscopy for stress characterization, and FEM modeling of ECM coupling effect.

1.1 Fundamentals of battery operation

In general, batteries are electrochemical devices that convert chemical energy into electrical energy through reduction-oxidation (redox) reactions. A typical battery is composed of two electrodes and an electrolyte. Each electrode is a half-cell that undergoes either oxidation or reduction reaction. The chemical energy associated with each redox reaction can be expressed as ΔG_r^0, the standard Gibbs free energy of the reaction, which defines an electrostatic driving force that balances the electroneutrality in the electrode:

$$E^0 = -\frac{\Delta G_r^0}{nF} \quad (1.1)$$

Where n is the number of electrons transferred in each redox reaction, F is Faraday constant, and E^0 is the standard potential of the electrode. The difference of E^0 between two electrodes defines the overall electrochemical cell potential of the battery:

$$E = E_+^0 - E_-^0 \quad (1.2)$$

Where E is the cell potential, E_+^0 and E_-^0 are the standard potentials of positive and negative electrodes. When the two electrodes are electrically connected through external circuit, the electrode that undergoes oxidation reaction, referred as negative electrode or anode, will release electrons from the electrode material into external circuit, while the opposite electrode that undergoes reduction reaction, referred as positive electrode or cathode, will receive electrons from the external circuit. This coupled redox process can be represented as following equations:

$$Anode: A \rightarrow A^{n+} + ne^- \quad (1.3)$$

$$Cathode: C^{n+} + ne^- \rightarrow C \quad (1.4)$$

$$Overall: A + C^{n+} \rightarrow A^{n+} + C \quad (1.5)$$

Where A is the anode and C is the cathode. As electrons continuously flow from anode to cathode, the anode is positively charged, while cathode is negatively charged. In order to balance the electroneutrality in the battery system, a third

component in the battery, referred as electrolyte, is needed. The electrolyte can provide and receive positive ions to balance the charge in both electrodes. The electrolyte is also an electrical insulator, to prevent internal short-circuit in the battery. In the end of discharge process, the standard potential of both electrodes approaches the same value, leading to a lower cell potential. For rechargeable batteries, or secondary batteries, the electron flow can be reverted in the presence of a power supply, which restores the chemical energy of the cell. The configuration and working principle of a typical battery are illustrated in figure 1.1.

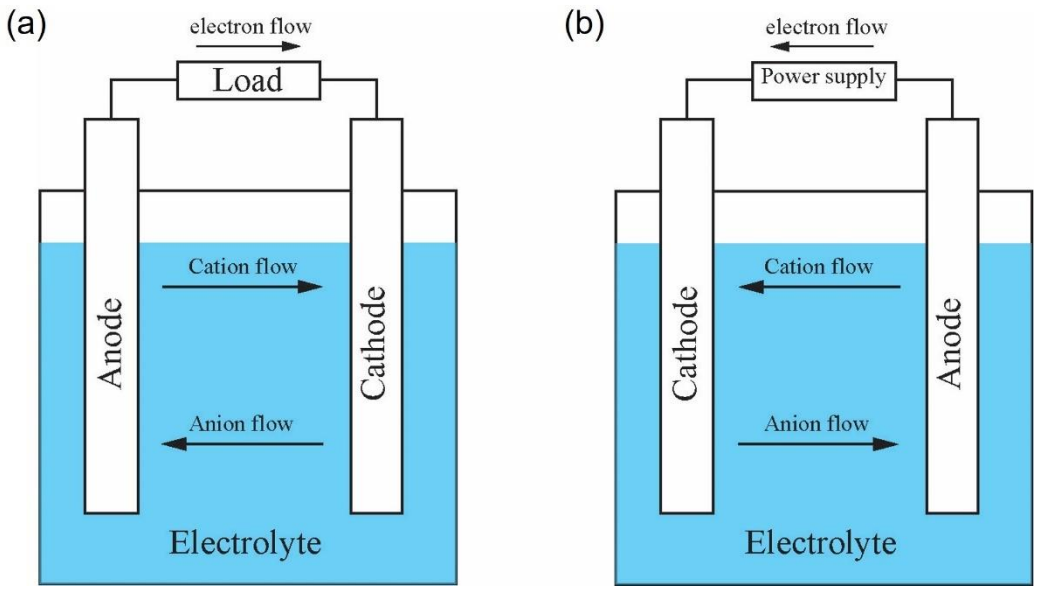

Figure 1. 1: Schematic of batteries in (a) discharge and, (b) charge process.

1.1.1 Li-ion batteries

Li-ion batteries, as the name suggests, use Li ions as positive ions to maintain the charge-neutrality in electrodes. In a typical Li-ion battery system, insertion-type

electrodes, like graphitic carbon anode and layered metal oxide cathode, are used, along with an organic Li containing electrolyte. The redox reactions of a typical Li-ion battery system with carbon anode and metal oxide cathode $LiCoO_2$ can be represented as following:

$$Anode: C + xLi^+ + xe^- \leftrightarrow Li_xC \quad (1.6)$$

$$Cathode: LiCoO_2 \leftrightarrow Li_{1-x}CoO_2 + xLi^+ + xe^- \quad (1.7)$$

$$Overall: LiCoO_2 + C \leftrightarrow Li_{1-x}CoO_2 + Li_xC \quad (1.8)$$

In this system, the redox reactions occurred at electrodes involve intercalation and de-intercalation of Li ions into or from the interstitial sites in the host structures. Consequently, minimal structural change in the electrodes is involved during charge and discharge processes, leading to facile and highly reversible electrochemical kinetics. In addition, the low mass of Li ions enables the high gravimetric and volumetric energy density of Li-ion batteries, making it a highly competitive ESD for applications in portable electronics and electric vehicles.

1.1.2 Solid-state Li-ion batteries

In traditional liquid-based LIBs, Li salts, typically $LiPF_6$ or $LiClO_4$, dissolved in organic solvents such as ethylene carbonate, dimethyl carbonate and propylene

carbonate, are used as electrolyte. However, the flammability and risk of thermal runaway of organic electrolytes cause serious safety concerns. Also, the limited electrochemical stability of organic liquid electrolyte eliminates the usage of Li metal electrode and thus, imposes a roadblock for further improvement of energy density of liquid-based LIBs. Alternatively, solid-state batteries use inorganic solid electrolytes, which provide better thermal and chemical stability than its liquid counterpart. The wider electrochemical stability window of solid electrolytes also enables the usage of high energy density electrodes without causing electrolyte degradation during cycling[7]. In addition, due to the mechanical rigidity, thickness of solid electrolyte can be reduced to a few hundred nanometers without introducing the risk of internal short-circuit and Li dendrite penetration through the electrolyte layer. Lastly, the discovery of fast ion-conducting solid electrolytes, such as LGPS and Nasicon type solid electrolytes[8,9], greatly reduced the overall impedance of solid-state batteries. Consequently, solid-state batteries are high energy and power density battery systems with improved safety comparing to traditional liquid-based LIBs. Although the exact physics at the solid electrode-electrolyte interface and the conduction mechanism of solid electrolyte aren't clear, and the mass production is still facing challenges, solid-state batteries represent the most promising route for the next generation high energy and power density LIBs.

1.2 Mechanical challenges of silicon electrode and stress characterization

Si is a promising electrode material for Li-ion batteries, due to its high theoretical energy density (4200mAh/g) and low working potential (0.1-0.4V). The abundance of Si in earth crust also lowers the cost of Si based LIBs. However, the application of Si electrodes in LIBs is facing serious mechanical challenges, since Si undergoes large volume change during Li insertion/extraction. The volume swing and the associated stress can cause mechanical problems in Si electrodes in a few aspects, as summarized in figure 1.2: First, deformed Si electrode after cycling can delaminate and detach from the current collector, leading to a larger electrode resistance. Second, cracks formed on the surface of Si electrode after cycling expos fresh Si for additional solid-electrolyte interface (SEI) formation, consuming extra Li ions in the battery system and leading to accelerated capacity fade[10]. Third, cracks propagate as cycling continues, which eventually causes pulverization of Si electrodes and complete isolation of Si electrode fragments[11,12], resulting in a catastrophic drop of battery capacity. Lastly, the stress induced by Li insertion/extraction also affects the diffusion and electrochemical kinetics in Si electrodes, leading to a coupled ECM effect[13]. Therefore, measuring the stress in Si electrodes during electrochemical cycling and understanding the ECM effect are critical for future design and application of Si electrodes in Li-ion batteries.

However, experimental study of ECM effect in Si is challenging. Lithiation kinetics of Si is sluggish, so typically, the lithiated Si layer only takes up a small fraction of the overall Si electrode. As a result, large gradient of Li concentration and lithiation associated stress develop. Spatially resolving the stress gradient in the Si electrode is thus the key for experimental study and understanding of ECM effect in Si electrode. Unfortunately, there are very limited numbers of techniques that can be applied to spatially resolve the stress in Si.

Figure 1. 2: Schematic of mechanical failure modes of c-Si electrodes

1.3 Raman spectroscopy

Raman spectroscopy is a spectroscopic technique that measures vibrational modes of molecules and is one of the few techniques that can measure stress distribution with high spatial resolution. In a light-matter interaction process, the incident electromagnetic wave creates charge separation, i.e. dipole moment, in molecules. Through molecular or lattice vibration, the dynamic variation of dipole

moment in turn generates inelastically scattered photons, and the frequency difference between the incident photon and inelastically scattered photons is reflected in Raman spectra. In this process, the energy conservation yields

$$\hbar\omega_s = \hbar\omega_i \pm \hbar\Omega \tag{1.9}$$

Where $\hbar\omega_i$ is the energy of incident photon, $\hbar\omega_s$ is the energy of scattered photon, and $\hbar\Omega$ corresponds to the energy transfer to the lattice vibration. For the process where $\hbar\omega_i$ is larger than $\hbar\omega_s$, it is called Stoke Raman scattering, while for process where $\hbar\omega_i$ smaller than $\hbar\omega_s$, it is called anti-Stoke Raman scattering.

In an analogy to energy conservation, momentum conservation of the scattering process yields relationship between incident photon wavevector k_i, scattered photon wavevector k_s, and wavevector of lattice vibration k_i:

$$\boldsymbol{k}_s = \boldsymbol{k}_i \pm \boldsymbol{q} \tag{1.10}$$

In a typical Raman measurement, the wavelength of incident laser (few hundreds nm) is much larger than the lattice constant of crystalline samples like Si ($a = 0.5nm$), so the phonon modes that are excited typically span over the entire lattice, i.e. $\boldsymbol{q} \approx 0$. Therefore, for crystalline materials, Raman spectroscopy essentially measures the optical phonon modes near the Γ point at the center of Brillouin zone. In the following sections, equipment configuration of Raman spectroscopy, μ-Raman stress measurement in Si, and application of Raman in electrochemical study of Si electrode will be presented.

1.3.1 Equipment configuration

Modern Raman spectroscopy, particularly micro-Raman spectroscopy, is composed of three major units: Laser source, microscope system, and a computer-controlled spectrometer system. The Raman laser beam with various wavelength can be generated by different laser sources, such as Argon gas, Helium Neon, and GaAs. The intensity of the laser is first tuned by an intensity filter and ported into a microscope system through mirrors and a beam splitter. The incident laser is then focused on the sample surface through an objective lens. In the backscattering configuration, the scattered light generated from the sample is passed into the same light path same as the incident laser, and the elastically scattered photons are filtered out by a Rayleigh filter (edge or notch filter). Next, a confocal hole is used to selectively filter light focused on the focal plan. The inelastically scattered light generated at the focal plan from the sample is then passed through an entrance slit. The diffracted light is collimated through a collimator and photons at different energy are spread out after passing a grating and eventually, collimated and passed into a CCD detector to form Raman spectra. The usage of high magnification objective lens and confocal hole, along with high precision XY stage, provide Raman a spatial resolution down to few hundred nm, while the usage of slit and

grating (600-2400 groove/mm) provide Raman with energy resolution down to 0.4 1/cm.

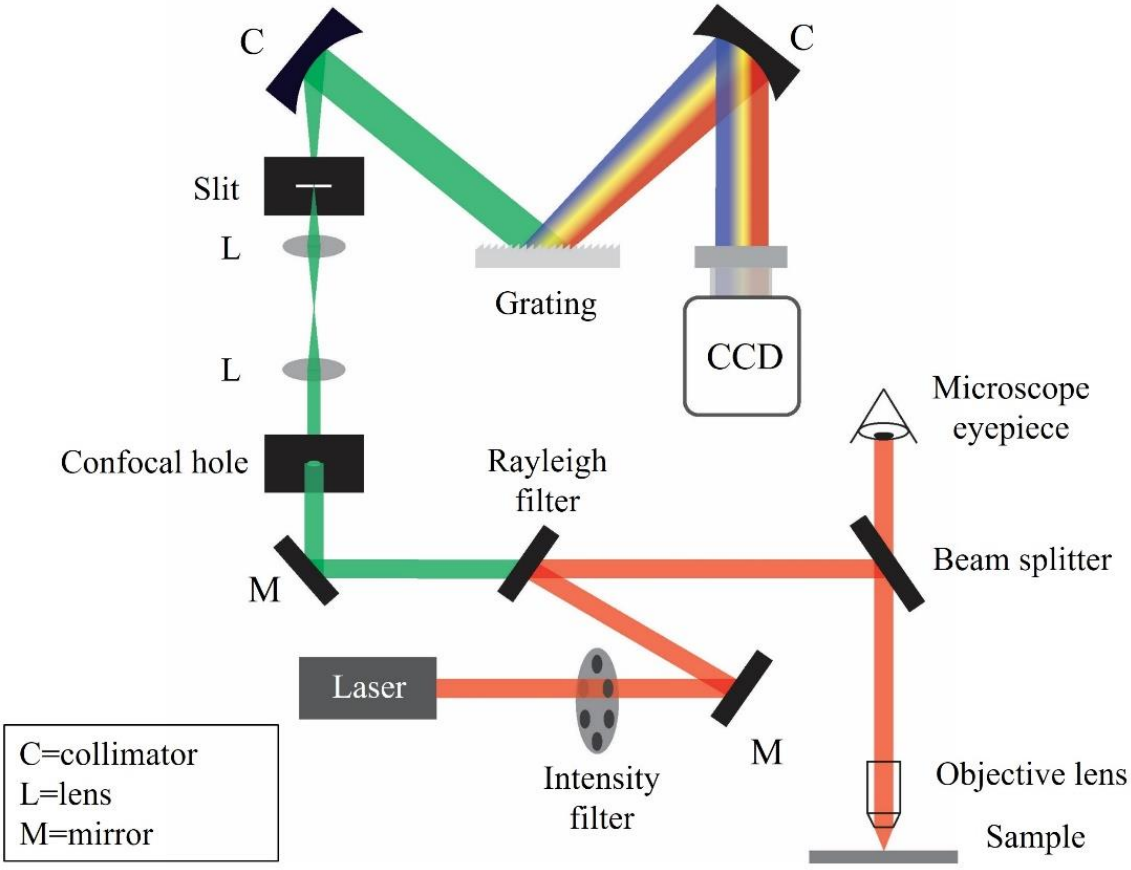

Figure 1. 3: Schematic of Micro-Raman equipment configuration

1.3.2 μ-Raman stress measurement in crystalline Si

Si lattice has a highly symmetric cubic structure, which gives rise to a triply degenerated optical phonon mode at the center of Brillouin zone[14], as shown in figure 1.3(a). The frequency of this phonon mode is 15THz, which converts to wavenumber of ~521cm^{-1}. Consequently, a sharp Raman peak of Si is centered at

~521cm^{-1} when the Si lattice is in stress-free state. When stress is applied to the Si lattice, the lattice constant changes and the phonon modes change frequency. The effect of stress on optical phonon modes in crystalline Si was first studied by Ganesan et al. and Anastassakis [15,16]. They found that in the presence of symmetric stress, the triple degeneracy of optical phonon modes at $k = 0$ is lifted, due to anisotropic change of lattice constants. Each of the strain-split phonons exhibit its own frequency, and for elastic deformation, Raman shift varies linearly with the stress. In general, tension stress causes Si Raman peak to shift to lower frequency, while compression does the opposite. In addition, due to the loss of degeneracy at center of Brillouin zone, the Raman peak shifts are usually accompanied with peak width change. Depending on the orientation of Si and Raman configuration, stress tensor components in Si can be resolved.

Ever since the discovery of correlation between stress and Raman shift in Si, μ-Raman spectroscopy has become a popular technique for stress characterization in Si based semiconductor devices [17,18]. A prior study of stress distribution in Si substrate induced by Si_3N_4 overlayer is shown in figure 1.3(c). In this study, resolution of Raman stress measurement is in the order of ~10MPa, and with high precision XY stage, the spatial resolution reached to ~200nm, which demonstrates a powerful capability of μ-Raman spectroscopy to resolve stress distribution in Si based structures.

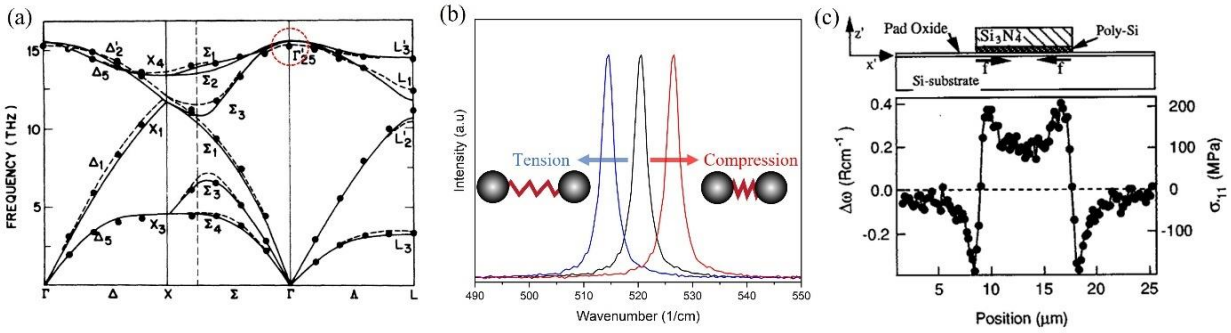

Figure 1. 4: (a) Phonon band structure of c-Si (Adapted with permission from [14]). (b) Schematic of Raman shift-stress correlation. (c) Micro-Raman stress measurement on Si substrate with poly-Si and Si_3N_4 overlay (Adapted with permission from [17]).

1.3.3 Raman application in Si electrodes

Although Raman spectroscopy is a powerful technique for stress measurement and has been used extensively on Si based semiconductor devices in the past, it has not been adopted widely in electrochemical studies of Si electrodes. Comparing to other stress characterization techniques such as multi-beam optical sensor (MOS), Raman spectroscopy is a direct measurement technique that probes the electrochemically active materials. This gives Raman a few challenges for in-situ Raman stress measurement of Si electrodes: First, Si electrodes has low working potential. The alloying reaction between Li and Si occurs at ~0.1V vs Li/Li^+. At this low potential, common organic liquid electrolytes are readily decomposed, and a SEI layer forms on the surface of Si electrode, which suppress the optical access of Raman laser to Si. This effect is demonstrated in a prior work, as shown in figure 1.4(a) [18]: During discharge process, the half-cell potential changed from 0.8V to

0.1V, while before the Si/Li alloying reaction occurred at 0.1V, the Si Raman peak intensity diminished and dropped to zero due to SEI layer formation on the surface of Si electrode.

Second, the penetration depth of Raman laser in Si is in the order of ~1um (0.7um for 532nm/3um for 633nm), while the movement speed of lithiation front in Si is typically ~100nm/hr [19,20]. This indicates that before a thick and stable SEI layer formed (<1hr) on the surface of Si, the thickness of Li_xSi layer and the associated stress field are only a small fraction of the probing depth of Raman laser. Consequently, a large average effect occurs in Raman measurement. Therefore, a successful Raman stress measurement in Si electrodes should involve: 1. Controlled SEI layer thickness. 2. Controlled probing depth in Si electrode. In this dissertation, a few different strategies will be used to overcome the challenge in Raman measurement of Si electrodes.

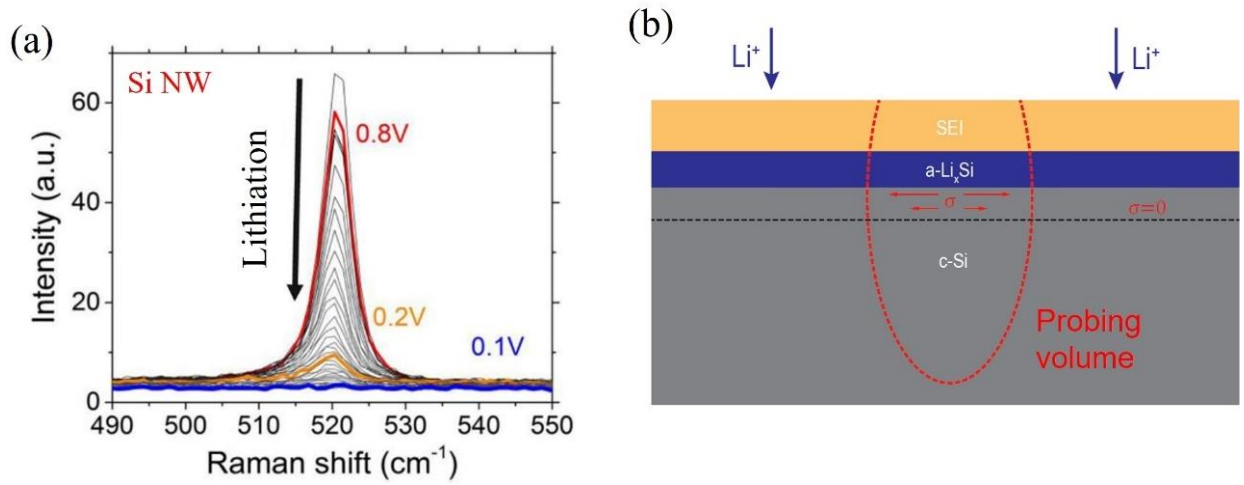

Figure 1. 5: (a) In-situ Raman measurement of Si electrode during half-cell discharging (Adapted with permission from [18]). (b) Schematic of stress average effect in Si electrode during Raman measurement.

1.4 Finite element modeling (FEM)

The laws of physics for space- and time-dependent problems are usually expressed in partial differential equations (PDEs). For vast majority of the engineering problems, solving the PDEs in an analytical manner is impractical, due to limitations of current mathematical tools. However, numerical solutions can be obtained by converting PDEs into a discrete system of algebraic equations. This process is called discretization. Several discretization methods exist, to discretize either time or spatial derivatives of PDEs. For FEM, spatial derivatives are obtained from PDEs, which makes it a powerful computational technique to solve physics problems that involve complex geometries. The numerical solutions of PDEs in each element construct the overall solution of the original physical system. The solution

is an approximate since numerical errors are introduced as the continuous differential terms in governing PDEs are replaced by algebraic expressions connecting nodal points between finite elements. FEA has become a powerful technique for battery research in the last few decades due to its capability to provide physical pictures for complex electrochemical systems. Si electrode modeling is one example where FEA is of critical use: During lithiation, the Si electrodes undergo phase transformation, and the stress generated from the lithiated Si phase imposes a strong tension at the phase boundary, which induces plastic deformation at the interface. The stress also regulates the diffusion process of Li in Si, which in turn affects the electrochemical kinetics at the interface (i.e. chemical potential is a function of concentration). Therefore, lithiation/delithation processes in Si electrodes involve multiple physics that interplay with each other. In the following sections, we will present a procedure for building electrochemo-mechanical model that is used in this dissertation.

1.4.1 Chemical diffusion

As a first order approximation, Li insertion into Si electrode is a solid mixing process. In general, the chemical potential of Li in a solid is expressed as

$$\mu_{Li} = \mu_0 + k_B T ln(c_{Li}) \tag{1.11}$$

Where μ_0 is chemical potential of free Li atoms, $k_B T$ is thermal energy, and c_{Li} is the normalized concentration of Li atoms. The gradient of chemical potential drives mass transport of Li, and the mass flux is given by

$$J = -M c_{Li} \nabla \mu_{Li} = -D \nabla c_{Li} \tag{1.12}$$

Where M is the mobility of Li atoms in the solid, and D is the diffusion coefficient of Li which is equal to $M k_B T$ based on Nernst Einstein equation. The time derivative of Li concentration is governed by Fick's second law

$$\frac{\partial c_{Li}}{\partial t} = -\nabla \cdot J = D \nabla^2 c_{Li} \tag{1.13}$$

Thus, Equation (1.13) is the governing equation of chemical diffusion model of Li in Si electrode.

1.4.2 Diffusion induced stress

Li insertion in Si causes volume change, and associated stress in turn affects the energy barrier for Li diffusion [21,22]. Thus, the chemical potential of Li in Si matrix needs to be modified

$$\mu_{Li} = \mu_0 + RT ln(c_{Li}) + \Omega P \tag{1.14}$$

Where Ω is the molar volume change of lithiated Si, and P is the pressure associated with lithiation. Plugging equation (1.14) into (1.12) and (1.13) lead to a modified governing equation for the diffusion process

$$\frac{\partial c_{Li}}{\partial t} = -D\nabla \cdot \left(\nabla c_{Li} - \frac{\Omega c_{Li}}{R\mathrm{T}} \nabla \mathrm{P}\right) \tag{1.15}$$

The volume change of Si induced by lithiation is reflected in strain tensor

$$\boldsymbol{\varepsilon} = \boldsymbol{\varepsilon^{el}} + \frac{\Omega}{3}\left(c_{Li} - c_{0,Li}\right) \tag{1.16}$$

Where $\boldsymbol{\varepsilon^{el}}$ attributed to the elastic deformation, and $\frac{\Omega}{3}\left(c_{Li} - c_{0,Li}\right)$ term is attributed to inelastic chemical deformation induced by Li concentration change with respect to reference molar concentration of Li.

The stress tensor can be expressed as a function of strain tensor

$$\boldsymbol{\sigma} = [2Gdev(\boldsymbol{\varepsilon}) + Ktr(\boldsymbol{\varepsilon})\mathbf{1}] - \mathrm{K}\Omega\left(c_{Li} - c_{0,Li}\right)\mathbf{1} \tag{1.17}$$

Where G and K are shear and bulk modulus of lithiated Si. The left term in (1.17) is a standard conversion between stress and strain tensor for elastic deformation, while the right term attributes to the inelastic deformation induced by lithiation.

To maintain force balance in the system, **linear momentum conservation** requires

$$\nabla \cdot \boldsymbol{\sigma} = 0 \tag{1.18}$$

Plugging equation (1.16) and (1.17) into (1.18) lead to

$$\nabla \cdot \left([2Gdev(\boldsymbol{\varepsilon}) + Ktr(\boldsymbol{\varepsilon})\mathbf{1}] - \mathrm{K}\Omega\left(c_{Li} - c_{0,Li}\right)\mathbf{1}\right) = 0 \tag{1.19}$$

Equation (1.15) and (1.19) thus form the governing equation system for the coupled chemo-mechanical model.

We demonstrate the effect of chemo-mechanical coupling in a simple 2D model, where a constant lithiation current is applied at front side of Si electrode(y=0), with bottom side mechanically fixed, as shown in figure 1.5(a). Li concentration in Si electrode along the red dashed line in 1.5(a) is shown in figure 1.5(b). The chemo-mechanical coupled model shows a smaller concentration gradient than pure chemical diffusion model, indicating that the tensile stress generated by lithiation increases the diffusivity and promotes Li diffusion. This stress-regulated diffusion enhances as the charge rate increases, as stronger stress gradient builds up inside the Si electrode.

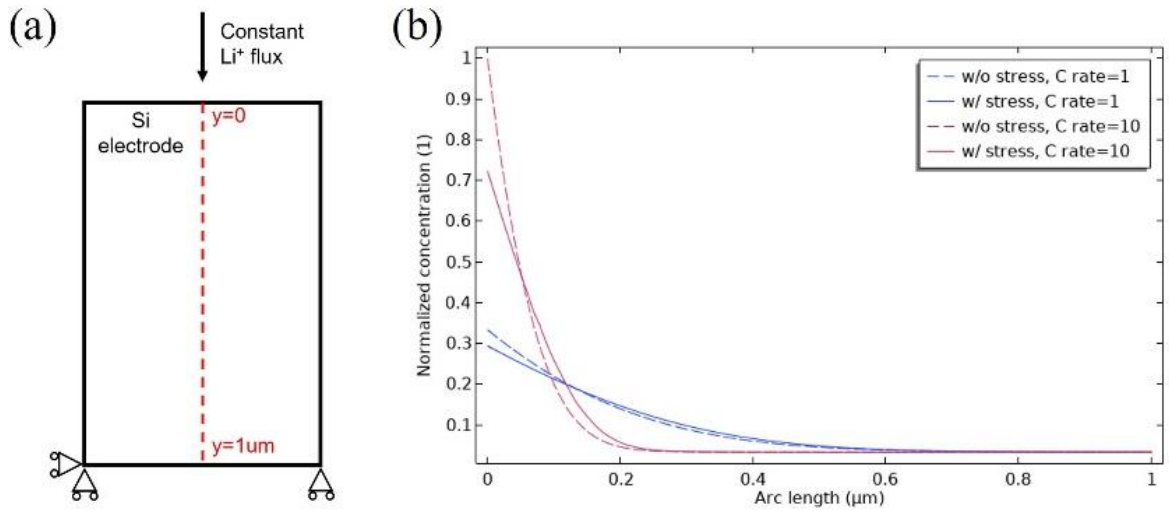

Figure 1. 6: (a) Boundary conditions of the 2D chemo-mechanical model. (b) Normalized concentration of Li in Si along the red dashed line in (a).

1.4.3 Stress-regulated surface charge transfer

Lastly, the stress induced by lithiation not only affects the free energy of Li atoms in Si electrode, but also the electrochemical kinetics of charge transfer across the electrode-electrolyte interface [13]. A typical energy scheme at electrode-electrolyte interface is shown in figure 1.6(a): At the interface, Li ions can be reduced into Li atoms, and vice versa. By controlling the electrical overpotential $(E - E_0)$, free energy of Li ions can be shifted, which affects the equilibrium of the redox reaction at the interface. This is the classical interface charge transfer correlation, described by Butler-Volmer equation:

$$i = i_0 \left\{ exp\left[(1-\alpha)\frac{F(E-E_0)}{RT} \right] - exp\left[\alpha \frac{F(E-E_0)}{RT} \right] \right\} \qquad (1.20)$$

Where i_0 is the exchange current density at equilibrium state, α is charge transfer coefficient, F is Faraday constant, $E - E_0$ is the electrical over-potential, and RT is the thermal energy.

When stress presents, however, the energy barrier for Li ions reduction further shifts as the free energy of Li atoms is affected by the mechanical stress $\sigma_m \Omega$. The effect of stress on the equilibrium potential of Si electrodes have been previously measured in experiments [23], with 1GPa stress changes the electrical potential by ~60mV. Therefore, the traditional charge transfer relationship is insufficient for ECM model, and a modified Butler-Volmer equation should be adopted:

$$i = i_0 \left\{ exp\left[(1-\alpha) \frac{F(E-E_0) - \sigma_m \Omega}{RT} \right] - exp\left[\alpha \frac{F(E-E_0) - \sigma_m \Omega}{RT} \right] \right\} \qquad (1.21)$$

Where σ_m is the molar volume expansion of Si lattice with Li insertion. Equations (1.13), (1.19) and (1.21) form the complete governing equation system for ECM modeling for Si electrodes.

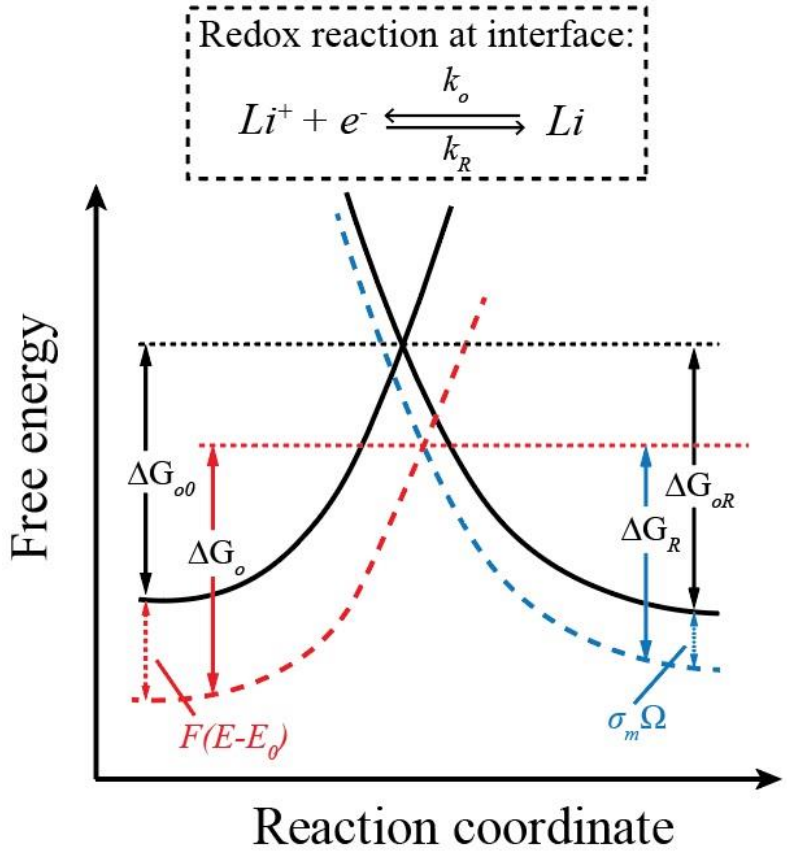

Figure 1. 7: Schematic of free energy shift at the electrode-electrolyte interface as a function of electrical overpotential and mechanical stress.

Chapter 2: Methods

This chapter provides an overview of the experimental and modeling procedures that are used as the basis of the work presented in the following chapters. The experimental part includes Si electrode preparation, electrochemical cell design, and sample characterization. The modeling part includes derivation of Raman shift-stress correlation and ECM models that are used for theoretical analysis of experimental results.

2.1 Fabrication techniques

In chapter four and five, model devices are fabricated using thin film deposition and patterning techniques. In this section, procedures for thin film deposition, photopatterning, and dry etching are elaborated.

2.1.1 Thin film deposition

2.1.1.1 W sputtering:

Tungsten films were deposited by DC magnetron sputtering (AJA, ATC-Orion 8) using a metallic W target (99.95% purity, 3 in. diameter). Before sputtering, the vacuum chamber was pumped to a base pressure of 5×10^{-8}Torr, and the distance between W target and the substrate was kept at 10cm. Plasma ignition was performed at 50W and 25mTorr with presence of 30sccm Ar gas. Substrate was isolated from the plasma by a shutter.

During deposition, the substrate temperature was kept at room temperature, while a constant pressure of 3mTorr was maintained in the presence of Ar process gas, flowed at 25sccm. A power of 300W was applied to the W target to maintain a bias voltage of ~150V. The deposition rate is ~24nm/min.

2.1.1.2 LiPON sputtering:

LiPON films were deposited by reactive RF magnetron sputtering (AJA, ATC-1800) using a Li_3PO_4 target (99.95% purity, 3 in. diameter) and N_2 gas. Before sputtering, the vacuum chamber was pumped to a base pressure of 1×10^{-7}Torr, and the distance between W target and the substrate was kept at 10cm. Plasma ignition was performed at ~10W and 25mTorr with presence of 20sccm Ar gas.

During deposition, Ar gas flow was switched off and the substrate temperature was kept at room temperature. A constant pressure of 2mTorr was maintained in the presence of N_2 reactive gas, flowed at 20sccm. A power of 100W was applied to the Li_3PO_4 target. The deposition rate is ~0.9nm/min.

2.1.1.3 Al_2O_3 sputtering:

Al_2O_3 films were deposited by RF magnetron sputtering (AJA, ATC-1800) using a Al_2O_3 target (99.99% purity, 3 in. diameter). Before sputtering, the vacuum chamber was pumped to a base pressure of 1×10^{-7}Torr, and the distance between Al_2O_3 target and the substrate was kept at 10cm. Plasma ignition was performed at

30W and 25mTorr with presence of 20sccm Ar gas. Substrate was isolated from the plasma by a shutter.

During deposition, the substrate temperature was kept at room temperature, while a constant pressure of 5mTorr is maintained in the presence of Ar process gas, flowed at 25sccm. A power of 200W was applied to the Al_2O_3 target to maintain a bias voltage of ~200V. The deposition rate is ~1.6nm/min.

2.1.1.4 ALD Al_2O_3 deposition:

Atomic layer deposition (ALD) of Al_2O_3 films was conducted in an ALD reactor (Beneq, TFS 500). Trimethyl-aluminum (TMA) and water were used as precursors for the thermal ALD process. Base pressure of 4mTorr was maintained before the ALD process begins.

During deposition, substrate temperature was kept at 150^{o}C and both precursors were vaporized at room temperature. For each ALD cycle, alternating TMA and water vapor pulses were injected into the reactor with Ar carrier gas for 200ms, and after each pulse, 500ms of purge was applied to remove residual precursor gases. The deposition rate is ~0.1nm/cycle.

2.1.1.5 LPCVD poly-c Si:

Poly-c Si thin films deposited through low pressure chemical vapor deposition (LPCVD) processes was conducted in a hot-wall LPCVD reactor (Tystar) using a gas mixture of Silane (SiH_4) and N_2. Thermal decomposition of Silane was

proceeded at 650ºC for deposition of poly-c Si thin films. The deposition rate is ~100nm/hr.

2.1.1.6 PECVD a-Si:

a-Si thin films deposited through plasma enhanced chemical vapor deposition (PECVD) were conducted in a CVD reactor (Oxford). High frequency (13.56MHz) power source with 20W forward power was applied to generate plasma. During deposition, mixture gas of 5%SiH_4/95%N_2 was flowed at 400sccm. The chamber pressure was maintained at 2000mTorr and substrate temperature was kept at 300ºC. The deposition rate is ~60nm/min and a-Si exhibited dark conductivity of ~10^{-10} to 10^{-12} S/cm.

2.1.2 Photolithography

The photolithography process starts with photoresist coating. First, an adhesion promotor HDMS was spin casted on substrates at 4000rpm for 60sec. Second, a positive photoresist (Shipley, 1813) was spin casted on the substrates at the same spin rate and time duration, and the coated substrate was soft-baked on a heat plate at 100ºC for 1 minute to promote adhesion of photoresist. Third, the substrates with photoresist were carried to a mask aligner (Karl Suss, MJB-3). Bright-field soda-lime masks were installed on the mask aligner and UV light with 365nm wavelength @ 8mW was used to cross-link the exposed photoresist. Total exposure time was

controlled to 7.5s for optimal feature resolution. Fourth, samples were rinsed in a photoresist developer (Shipley, CD-26) for 30 second to develop the exposed photoresist. Lastly, samples were rinsed in a water bath and blown dry by a high-pressure Argon gun.

2.1.3 Reactive ion etching

Reactive ion etching (RIE) was performed in a ICP etcher (Oxford). During etching process, plasma was first generated through a RF power supply with 500W. Then, a gas mixture of 10sccm O_2, 50sccm Ar, and 50sccm CF_4 was flew into the chamber, and 50W power was applied to the second RF power supply to maintain a bias voltage of ~150V on the substrate. 40mTorr chamber pressure and 20^{o}C substrate temperature were maintained during the etching process. The etching recipe was used for etching of W (etch rate: ~1nm/s), poly-c Si (etch rate:~1.2nm/s), and a-Si (etch rate:~3nm/s). The etching recipe was not optimized for selectivity, and for multi-layer structure etching, visual examination was used to determine the end of etching process.

2.2 Electrochemical cell design

Throughout this dissertation, custom-made electrochemical cells with different architectures were fabricated for ex-situ and in-situ Raman measurement. In this section, details of cell fabrication and assembly process are presented.

2.2.1 Liquid cell for ex-situ study

Design of the liquid electrochemical cell used for ex-situ Raman study is shown in figure 2.1(a). The cell is composed of four parts: a metal cap, glass cover, cell body, and a stainless-steel (SS) screw. The single c-Si electrodes obtained from wafer chip was placed on the SS screw and tightened against the cell body. The cell body is made of high-density polyethylene (HDPE). Li metal foil was molded and placed inside a small groove that connects to a SS screw from the side. Liquid electrolyte 1M $LiClO_4$/propylene carbonate (PC) was then used to fill the empty space in the cell. Lastly, glass cover was placed on top of the cell body and a metal cap was used to seal the cell.

2.2.2 Liquid cell for in-situ study

Design of the liquid electrochemical cell used for in-situ Raman study is shown in figure 2.1(b). The cell is composed of four parts: a metal cap, glass cover, upper and lower cell body. To accommodate the short working distance of objective lens used for in-situ Raman study, the Si electrode was placed in the upper cell chamber,

and Li metal foil is placed at the lower cell chamber. In both chambers, a SS screw from the side is used for electrical connection to the electrodes. Similar electrolyte filling and cell sealing procedure are applied in this cell as in the ex-situ electrochemical cell.

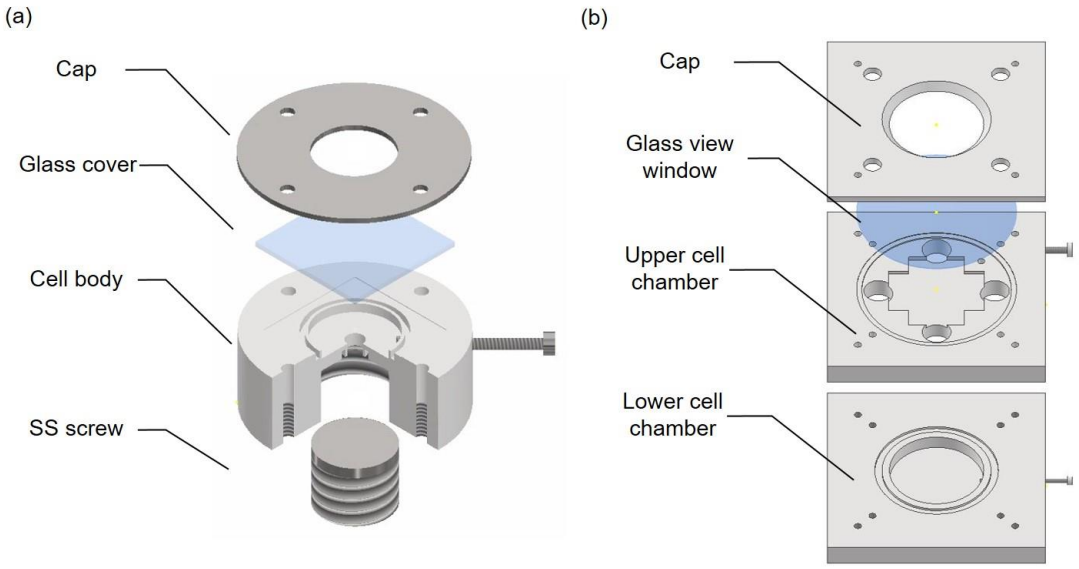

Figure 2. 1: Schematic of electrochemical cells for (a) ex-situ Raman study, and (b) in-situ Raman study.

2.3 Characterization techniques

In this section, equipment and techniques that were repeatedly used for sample imaging and characterization are presented.

2.3.1 Electrochemistry

Electrochemistry testing, including galvanostatic charge/discharge (GCD), cyclic voltammetry (CV), and electrochemical impedance spectroscopy (EIS), was

performed on a potentiostat (Bio-Logic, VSP). A low current channel was utilized during the electrochemical testing of solid-state battery platforms in chapter five, to enable current measurement down to 1nA with resolution of 80fA.

2.3.2 Scanning electron microscopy

A dual beam scanning electron microscopy (SEM) system (Tescan, GAIA) equipped with field emission gun was used for SEM imaging. During operation, base pressure of SEM chamber was kept at ~10^{-6} Torr. 10kV acceleration voltage was applied to incident electron beam and an in-beam secondary electron detector was used to generate SEM images. Energy dispersive spectroscopy (EDS) and electron backscattered diffraction (EBSD) results were also obtained from this SEM system.

2.3.3 μ-Raman spectroscopy

Raman spectroscopy measurement was carried out on a μ-Raman system (Horiba Jobin Yvon, Model HR800). Two incident laser sources (HeNe @ 633nm and GaAs @ 532nm) were equipped on the system. During Raman measurement, samples were mounted on a motorized XY stage with step resolution of 100nm. Pinhole size of 400um and slit size of 100um along with grating of 1800/cm were used. For peak reference, Si Raman peak of an undoped single-c Si chip was measured and calibrated to wavenumber 520.7 1/cm before every Raman experiment.

2.4 Theoretical calculation and modeling

In this section, correlation between Raman shift and stress in Si is derived and the framework of FEM model with ECM coupled physics is presented.

2.4.1 Raman shift-stress relationship

In light-matter interaction, electromagnetic wave creates a dipole in materials. The dynamic dipole moment variation, or the dynamic separation of charges in the material give rise to inelastically scattered photons, which are measured by Raman spectrometer. In this scenario, some inelastically scattered photons are not visible depending on the orientation of the sample and detector. Therefore, to calculate the Raman shift-stress relationship, visible Raman mode needs to be evaluated first. In the following sections, visible Raman mode for backscattering Raman configuration, Raman frequency shift in reference coordinate system, and Raman shift-stress correlation are derived. Here, we use (110) Si as an example (applied to chapter 3 and chapter 4) for the derivation.

2.4.1.1 Selection rule and visible Raman mode:

The Raman polarizability tensors of Si in the reference coordinate system with axes [1,0,0], [0,1,0], and [0,0,1] are well-studied [24], given as:

$$R_1 = \begin{pmatrix} 0 & 0 & 0 \\ 0 & 0 & 1 \\ 0 & 1 & 0 \end{pmatrix}$$

$$R_2 = \begin{pmatrix} 0 & 0 & 1 \\ 0 & 0 & 0 \\ 1 & 0 & 0 \end{pmatrix}$$

$$R_3 = \begin{pmatrix} 0 & 1 & 0 \\ 1 & 0 & 0 \\ 0 & 0 & 0 \end{pmatrix}$$

Where x, y, and z correspond to [1,0,0], [0,1,0],and [0,0,1] directions respectively.

For (110) Si, Raman polarizability tensors in the sample coordinate system can be obtained through coordinate transformation and are calculated:

$$R_{1'} = \frac{1}{\sqrt{2}} \begin{pmatrix} 0 & 0 & 1 \\ 0 & 0 & 1 \\ 1 & 1 & 0 \end{pmatrix}$$

$$R_{2'} = \frac{1}{\sqrt{2}} \begin{pmatrix} 0 & 0 & 1 \\ 0 & 0 & -1 \\ 1 & -1 & 0 \end{pmatrix}$$

$$R_{3'} = \begin{pmatrix} 0 & 1 & 0 \\ 1 & 0 & 0 \\ 0 & 0 & 0 \end{pmatrix}$$

Where 1, 2, and 3 denotes [1,1,0], [-1,1,0],and [0,0,1] axes for the sample coordinate system.

Raman scattering intensity is given by the selection rule:

$$I = C \sum_j \left| e_i \cdot R_j \cdot e_s \right|^2 \qquad j = 1', 2', or\ 3' \tag{2.1}$$

Where C is a constant, R_j is the Raman polarizability tensor, and e_i and e_s are polarization vectors of incident and scattered light. For Raman spectroscopy with backscattering configuration, equation (1) indicates that only $R_{3'}$ is active.

2.4.1.2 Raman frequency shift in reference system:

Silicon, when stress free, has triply degenerated phonon mode at the center of Brillion zone (q=0). This degeneracy is lifted in the presence of stress, and the frequency of each phonon modes (two transverse, one longitudinal) is given [25]

$$\sum_{\beta} K_{\alpha\beta}\eta_{\beta} = \omega^2\eta_{\alpha} \qquad \alpha,\beta = 1-3 \tag{2.2}$$

Where η_{α} are eigenvectors, ω is the Raman mode frequency under strain, and $K_{\alpha\beta}$ are elements of the force constant tensor which are given as

$$K_{\alpha\beta} = K_{\alpha\beta}^{(0)} + \sum_{vu} \epsilon_{vu} K_{vu\alpha\beta}^{(\epsilon)}, \qquad K_{\alpha\beta}^{(0)} = \omega_0^2 \delta_{\alpha\beta} \tag{2.3}$$

$\delta_{\alpha\beta}$ is Kronecker delta, and ϵ_{vu} and $K_{vu\alpha\beta}^{(\epsilon)}$ are strain tensor components and force constant tensor components in the reference coordinate system. For silicon, $K^{(\epsilon)}$ is highly symmetric and only has three independent components

$$\begin{aligned} K_{aaaa}^{(\epsilon)} &= p \\ K_{aabb}^{(\epsilon)} &= q \\ K_{abab}^{(\epsilon)} &= r \end{aligned} \tag{2.4}$$

Where $p, q, and\ r$ are known constants obtained from previous work[26]:

$$p/\omega_0^2 = -1.85, \qquad q/\omega_0^2 = -2.31, \qquad r/\omega_0^2 = -0.71,$$

Equation (2) can be fully expanded by using equations (3)-(4), and a secular equation in the reference coordinate system is derived:

$$\begin{vmatrix} p\epsilon_{11} + q(\epsilon_{22} + \epsilon_{33}) - \lambda & 2r\epsilon_{12} & 2r\epsilon_{13} \\ 2r\epsilon_{12} & p\epsilon_{22} + q(\epsilon_{11} + \epsilon_{33}) - \lambda & 2r\epsilon_{23} \\ 2r\epsilon_{13} & 2r\epsilon_{23} & p\epsilon_{33} + q(\epsilon_{11} + \epsilon_{22}) - \lambda \end{vmatrix} = 0 \quad (2.5)$$

Where $\lambda = \omega^2 - \omega_0^2$

Solving secular equation (5) gives the full relationship between strain and Raman shift. However, assumptions need to be made on the mechanical conditions of studied materials to solve this equation. In our characterization, uniaxial stress (Ex-situ experiment, chapter 3) and biaxial stress (In-situ experiment, chapter 4) conditions are considered.

2.4.1.3 Raman shift-stress correlation:

For **uniaxial stress** in the sample coordinate system, the stress tensor components in the reference coordinate system can be transformed and calculated:

$$\sigma_{ij} = \begin{bmatrix} \frac{\sigma_{xx}}{2} & -\frac{\sigma_{xx}}{2} & 0 \\ -\frac{\sigma_{xx}}{2} & \frac{\sigma_{xx}}{2} & 0 \\ 0 & 0 & 0 \end{bmatrix} \quad (2.6)$$

The strain in the reference system is thus given as

$$\varepsilon_{ij} = \begin{bmatrix} \frac{(S_{11}+S_{12})}{2}\sigma_{xx} & -\frac{S_{44}}{2}\sigma_{xx} & 0 \\ -\frac{S_{44}}{2}\sigma_{xx} & \frac{(S_{11}+S_{12})}{2}\sigma_{xx} & 0 \\ 0 & 0 & S_{12}\sigma_{xx} \end{bmatrix} \quad (2.7)$$

Where S_{ij} are components of compliance matrix of Si, with $S_{11} = 7.68\ TPa^{-1}$, $S_{12} = -2.14\ TPa^{-1}$, and $S_{44} = 12.6\ TPa^{-1}$[27].

Plugging strain components into secular equation (5), the eigenvalues can be obtained:

$$\lambda_1 = \frac{1}{2}[p\sigma_{xx}(S_{11}+S_{12}) + p\sigma_{xx}(S_{11}+3S_{12}) + r\sigma_{xx}S_{44}]$$

$$\lambda_2 = \frac{1}{2}[p\sigma_{xx}(S_{11}+S_{12}) + p\sigma_{xx}(S_{11}+3S_{12}) - r\sigma_{xx}S_{44}]$$

$$\lambda_3 = [q(S_{11}+S_{12}) + pS_{12}]\sigma_{xx}$$

Since only the backscattered phonon mode is contributing to the Raman signal, the frequency shift that's measured in this experiment is correlated to the strain through:

$$\Delta\omega = \frac{\lambda_3}{2\omega_0} = \frac{[q(S_{11}+S_{12}) + pS_{12}]\sigma_{xx}}{2\omega_0} \quad (2.8)$$

The Si under study has $\omega_0 = 521.5cm^{-1}$, so

$$\Delta\omega = -2.3\sigma_{xx} \quad (2.9)$$

Where σ_{xx} has unit of GPa.

For **biaxial stress** in the sample coordinate system ($\sigma_{xx} = \sigma_{yy} = \sigma_I/2$), the stress tensor components in the reference coordinate system can be transformed and calculated:

$$\sigma_{ij} = \begin{bmatrix} \sigma_I & 0 & 0 \\ 0 & \sigma_I & 0 \\ 0 & 0 & 0 \end{bmatrix} \tag{2.10}$$

Then, strain tensor in the reference coordinate system:

$$\varepsilon_{ij} = \begin{bmatrix} \frac{(S_{11}+S_{12})}{2}\sigma_I & 0 & 0 \\ 0 & \frac{(S_{11}+S_{12})}{2}\sigma_I & 0 \\ 0 & 0 & S_{12}\sigma_I \end{bmatrix} \tag{2.11}$$

Plugging strain components into secular equation (5), the eigenvalues can be obtained:

$$\lambda_1 = (p+q)\frac{(S_{11}+S_{12})}{2}\sigma_I + qS_{12}\sigma_I$$

$$\lambda_2 = (p+q)\frac{(S_{11}+S_{12})}{2}\sigma_I + qS_{12}\sigma_I$$

$$\lambda_3 = q(S_{11}+S_{12})\sigma_I + pS_{12}\sigma_I$$

Where only λ_3 is visible. Thus, Si Raman peak frequency shift as a function of stress is expressed as

$$\Delta\omega = \frac{\lambda_3}{2\omega_0} = \frac{[q(S_{11}+S_{12}) + pS_{12}]\sigma_I}{2\omega_0} \tag{2.12}$$

So

$$\Delta\omega = -2.3\sigma_I \quad (2.13)$$

Where σ_{xx} has unit of GPa.

2.4.2 FEM modeling

A 2D time-dependent FEM model with ECM coupled physics was built for stress analysis. Implementation of the model was performed on COMSOL Multiphysics, using General Form PDE module. In the following sections, balance equations and constitutive equations that are used in the ECM model are elaborated.

2.4.2.1 Balance equations:

The ECM model was mainly applied in chapter four, where in-situ Raman measurement using liquid half-cell was conducted. In a typical model scheme that represents electrochemical half-cell with Si working electrode, as shown in figure 2.2, Li ions are reduced into Li atoms at the electrode-electrolyte interface. Then, Li atoms diffuse into Si electrode and expand Si lattice. In this model, a few assumptions were made: 1. Li supply from the counter electrode (Li metal) is infinite. 2. Electrochemistry kinetics of the cell is mainly limited by the Si electrode. 3. Polarization effect in electrolyte is minimal. Consequently, the ECM model was simplified and included only Si electrode with surface electrochemistry.

Three field variables were solved in the ECM model: u (displacement along x direction), v (displacement along y direction), and c (concentration of Li atoms). The overpotential at interface was also obtained by solving the interface reaction equation. In the model system, mass and force must balance, which lead to two balance equations that govern the entire model:

First, mass conservation:

$$\frac{\partial c}{\partial t} = D\nabla \cdot h_{Li} \tag{2.14}$$

Where D is diffusion coefficient and h_{Li} is flux of Li.

Second, linear momentum conservation:

$$\nabla \cdot \boldsymbol{\sigma} = 0 \tag{2.15}$$

2.4.2.2 Constitutive equations

Chemical potential of Li is expressed as

$$\mu_{Li} = \mu_0 + RTln(c_{Li}) + \Omega P \tag{2.16}$$

Where Ω is the molar volume of Li in Si, and P is pressure induced by lithiation. In solid mixing process, flux of Li is proportional to the gradient of chemical potential

$$h_{Li} = \mathrm{M}\nabla\mu_{Li} \tag{2.17}$$

Where M is mobility and can be correlated to diffusion coefficient D through Einstein relation

$$\mathrm{M} = \frac{\mathrm{D}}{\mathrm{RT}} \tag{2.18}$$

Thus, plugging (2.16) and (2.18) into (2.17) lead to

$$h_{Li} = \nabla c_{Li} - \frac{\Omega c_{Li}}{RT} \nabla \mathrm{P} \tag{2.19}$$

In the 2D ECM model, **plane strain** condition was assumed. Thus, strain tensor components are defined as

$$\varepsilon_{11} = \frac{\partial u}{\partial x}$$

$$\varepsilon_{22} = \frac{\partial v}{\partial y}$$

$$\varepsilon_{33} = 0$$

$$\varepsilon_{12} = \left(\frac{\partial u}{\partial y} + \frac{\partial v}{\partial x}\right)/2$$

Stress tensor can be converted from strain tensor through

$$\boldsymbol{\sigma} = 2Gdev(\boldsymbol{\varepsilon}) - \mathrm{P}\mathbf{1} \tag{2.20}$$

Where G is shear modulus and P is pressure.

In the ECM model, pressure is composed of two parts, elastic deformation and inelastic deformation induced by chemical diffusion:

$$P = -\frac{tr(\boldsymbol{\sigma})}{3} = -Ktr(\boldsymbol{\varepsilon}) + K\Omega\left(c_{Li} - c_{Li,0}\right) \tag{2.21}$$

Where K is bulk modulus.

Plugging equation (2.21) into (2.20) leads to a fully resolved stress tensor:

$$\sigma_{11} = \frac{2}{3}G(2\varepsilon_{11} + \varepsilon_{22}) + K\left[\varepsilon_{11} + \varepsilon_{22} + \varepsilon_{33} - \Omega\left(c_{Li} - c_{Li,0}\right)\right] \quad (2.22)$$

$$\sigma_{22} = \frac{2}{3}G(\varepsilon_{11} + 22\varepsilon_{22}) + K\left[\varepsilon_{11} + \varepsilon_{22} + \varepsilon_{33} - \Omega\left(c_{Li} - c_{Li,0}\right)\right] \quad (2.23)$$

$$\sigma_{33} = K\left[\varepsilon_{11} + \varepsilon_{22} + \varepsilon_{33} - \Omega\left(c_{Li} - c_{Li,0}\right)\right] \quad (2.24)$$

$$\sigma_{12} = 2G(\varepsilon_{12}) \quad (2.25)$$

Lastly, Faradaic current density at the interface is expressed by Butler-Volmer equation:

$$i = i_0\left[\exp\left(\frac{\alpha F\eta}{RT}\right) - \exp\left(-\frac{(1-\alpha)F\eta}{RT}\right)\right] \quad (2.26)$$

Where i_0 is exchange current at thermal equilibrium condition, α is transfer coeffieicnt, and η is overpotential that includes both electrical and mechanical terms. The exchange current i_0 is expressed as

$$i_0 = F\left[k_c c_{Li^+}\left(1 - \frac{c_{Li}}{c_{Li,max}}\right)\right]^{\alpha}\left(k_a\frac{c_{Li}}{c_{Li,max}}\right)^{(1-\alpha)} \quad (2.27)$$

Where k_c and k_a are transfer coefficient for cathodic and anodic reaction. Overpotential is expressed as

$$\eta = F(E - E_0) - \sigma_m\Omega \quad (2.28)$$

Combining equations (2.14) and (2.19) gives governing equation for mass conservation, equations (2.15) and (2.22)-(2.25) for linear momentum conservation, and (2.26)-(2.28) for interface electrochemical kinetics. In summary, full expression

for mass conservation, linear momentum conservation, and interfacial Faradaic current density forms the governing equations system that define the ECM model.

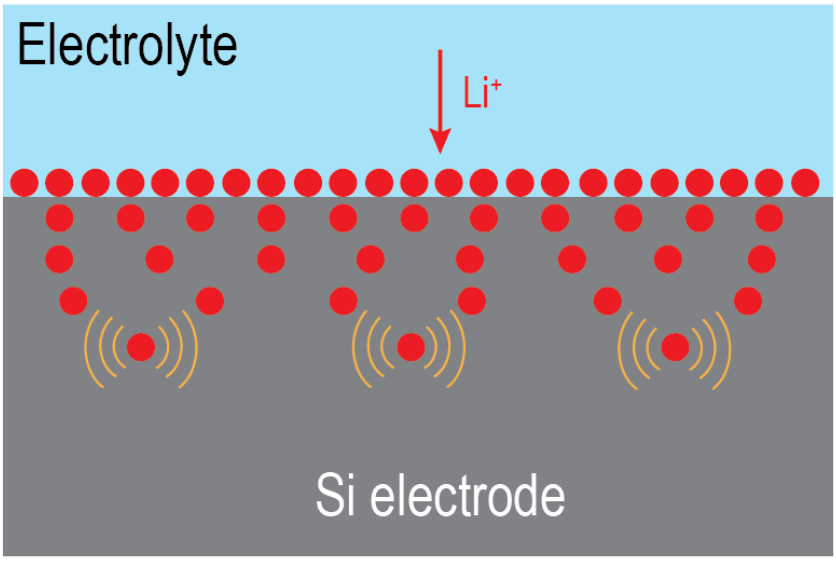

Figure 2. 2: Model scheme of half-cell with Si working electrode.

Chapter 3: Ex-situ stress characterization of single crystalline Si electrodes

3.1 Introduction

In the last decade, Si electrode has attracted much attention due to its high energy density and low working potential. However, slow kinetics of lithium diffusion in Si limits the practical energy density of bulk Si electrodes. During lithiation, the gradient of Li is accompanied with gradient of stress, which introduces various mechanical issues in Si electrode, leading to accelerated capacity fading of LIBs[28]. To improve the electrochemical and mechanical performance of Si electrode, novel structures have been developed, such as nanoparticles, double-walled hollow tubes, core-shell structures, and yolk-shell structures [29-35]. The nano-sized Si electrodes showed high energy density that is close to theoretical value and structural integrity even after hundreds of cycles. The invention of these electrodes, however, was largely driven by theoretical modeling. Experimental characterization of stress development in Si electrode, especially Si electrode with advanced geometries, is thus extremely valuable for theoretical understanding and advancement of Si-based LIBs.

Currently, Multi-beam optical sensor (MOS) has played the primary role on stress characterization in Si electrodes. In a typical MOS experiment, parallel laser beams are projected on the backside of Si substrate. Change of wafer curvature is measured during lithation/delithiation of Si electrodes and the stress in the surface

reacted layer is calculated from the curvature change using Stoney equation. This technique provided a foundation for stress measurement in Si electrodes, as some of the important stress effects have been found in previous MOS studies [36-38] . For both crystalline Si electrodes and amorphous Si thin film electrodes, stress plateau appears during lithation/delithaiton processes, revealing that the elastic to plastic transformation of lithiated Si and plastic flow at the interface between a-Li_xSi and Si are universal for Si electrodes. In this case, a large stress gradient is developed from lithiation front to the bulk of unlithaited c-Si. However, MOS can't measure stress distribution as it doesn't provide any spatial mapping capability. This disadvantage further limits the application of MOS in more advanced Si electrodes where stress heterogeneity becomes increasingly important for mechanical performance of the electrode[39-41]. Thus, stress characterization techniques that can provide scanning capability with resolution down to submicron will play a key role in future stress studies of Si electrodes.

μ-Raman spectroscopy, in combination with high magnification objective lens and confocal apertures, can provide spatial resolution down to a few hundred nanometers. Different from MOS, Raman spectroscopy directly probe the surface of electrochemically reacted Si, and the stress in Si lattice is reflected in the shift of Raman scattering frequency. So far, only a handful of Raman study has been done on Si electrodes [42-45]. In one work, In-situ Raman stress measurement on Si

nanoparticle electrodes was performed [42]: during lithiation, shift of Si Raman peak to lower frequency was observed as Li inserts into surface oxide, creating up to 0.2GPa tensile hoop stress on the inner c-Si core. As the lithiation front proceeds to the inner core region, Si Raman peak undergoes the opposite shift as compressive stress generated at the phase boundary starts to dominate. Raman measurement on c-Si wafer electrode and Si nanowires have also been reported [44,45], but detailed stress analysis was missing. For Si electrode, in-situ Raman study can be challenging, since the organic SEI layer and a-Li_xSi layer formation at low cell potential can block Raman laser from reaching c-Si and thus lose Raman signal. Therefore, detailed Raman study on Si electrodes needs careful design of experiment setup.

In this chapter, the application of μ-Raman in stress characterization of Si electrodes is demonstrated. As a proof of concept, we performed ex-situ μ-Raman study to investigate the stress distribution along the cross section of single c-Si electrodes. A few important findings have been pointed out in this work: First, the phase heterogeneity in lithiated c-Si electrode was studied by SEM and a three-layer structure, instead of two layers predicted prior studies, was observed. With help from characterization techniques such as SEM, EDS, EBSD, and XPS depth profile, we conclude that the formation of the extra c-Li_xSi layer at between a-Li_xSi and c-Si layers is probably due to the mechanical constraint imposed on the Si electrode in

our electrochemical cell. Second, the stress distribution in Si electrodes after initial lithiation were examined by Raman measurement, and a plastic deformation was observed at the phase-boundary. The flow stress at the phase boundary was measured and its magnitude showed linear relationship with lithiation capacity, which is consistent with a prior MOS study. Third, single-c Si electrodes after initial delithiation and additional cycling were studied by μ-Raman and SEM. Two different crack patterns were observed as cycling conditions change, and the corresponding fracture mechanism was proposed.

3.2 Experimental

3.2.1 Sample preparation

Single-c Si electrodes were obtained from single c-Si wafers. Primary grade wafers with orientation [001] and 500um thickness were purchased from University Wafer. The wafers are doped with phosphorous (n-type), and the electrical conductivity is between 1 to 10 $\Omega \cdot cm$. The single-c Si wafers were diced into small squares with approximate size of 8 by 8 mm. Before electrochemical treatment, the Si chips were rinsed in acetone, isopropanol, ethanol and water to clean the surface. The chips were then blown by a high-pressure air gun and dried in a vacuum load lock before being transferred into a glovebox with controlled O_2 and H_2O environment (concentration<0.1ppm) and assembled in an electrochemical cell.

After electrochemical treatment, electrochemical cells were dissembled in the same glovebox and Si chips were cleaned by DMC solution.

3.2.1 Electrochemistry

Galvanostatic discharge/charge using constant current of 10uA (~22uA/cm^2) have been conducted to electrochemically lithiate/delithiate the Si electrodes. For discharge process, the set point of potential was 10mV, while the cell potential never reached that value. Different discharging time, from 4hrs to 34hrs, was carried out to achieve different total lithiation capacity. For charge and cycling process, the setpoint potential for charging step was always set to 1.4V.

3.2.2 Electron beam microscopy and spectroscopy measurement

Single-c Si electrodes after electrochemical charge/discharge are removed from ex-situ Raman cell in a glovebox under controlled O_2 and H_2O environment (<0.1ppm). The samples were cleaned with DMC solution and left on Kim wipes to dry. Then, the Si electrodes were cleaved in half and mounted on a cubic metal stage using carbon tape. Lastly, the cubic stage with Si electrodes was placed in a vacuum box and carried over to SEM for imaging, EDS, and EBSD characterization.

3.2.3 μ-Raman spectroscopy

Single-c Si electrodes after electrochemical reactions were processed in the same procedure as used in section 3.2.2. The cleaved Si electrodes were mounted on a

vertical stage which sits in an air-tight cell. The cell was then transferred outside the glovebox and carried to Raman spectroscopy and mounted on a XY stage for Raman measurement. During Raman experiment, long working distance 50X objective lens with NA 0.5 (Olympus, LMPlanFl) was used. 532nm laser combined with D1 intensity filter and 0.5 second exposure, were used for each acquisition. The total energy for each acquisition was thus 0.8mW. For Raman scanning and mapping, 0.5um spacing was used.

3.2.4 X-ray photoelectron spectroscopy (XPS)

Single-c Si samples were transferred directly from the glovebox to the XPS chamber through a UHV loadlock system. The XPS (Kratos Ultra DLD system) characterization was performed with charge neutralization using a 12 kV monochromatic Al K X-ray source. High resolution spectra of O 1s, C 1s, Si 2p and Li 1s were collected with 0.1 eV step size and 20 eV pass energy. The XPS data were analyzed in CasaXPS. Depth profiles were performed using an Ar ion beam with a 5 kV accelerating voltage. The beam was rastered over a 2 mm x 2 mm area, while the XPS was collected from a spot 0.5 mm in diameter at the center of the etch crater.

3.3 Results and discussion

3.3.1 Initial lithiation of single c-Si electrodes

During the initial discharge process, the cell potential quickly dropped from OCV at ~2.8V to ~90mV and then, reclined to above 0.1V and stabilized at ~0.1V. The extensive lithiation plateau occurred at 0.1V was attributed to alloying reaction between Li and Si [46,47]. Single c-Si electrodes with different lithiation capacity, 93, 186, 373, and 930 uAh/cm^2, were studied. The cross-sectional SEM image of lithiated Si electrodes is shown in figure 3.1(a), where three layers with two interfaces are clearly observed. EDS line scan along the cross section of Si electrode shows that all three layers are composed of Si. Based on the line scan result, Si concentration is the lowest but stable in the top layer, and varies in the intermediate layer, then reaches a stable, higher level in the bulk unlithiated c-Si. Small amount of C and O and trace amount of Cl near the surface of sample indicates that air exposure was limited, and SEI layer was readily removed. In addition, Single-c Si electrodes at all lithiation capacity showed the same three-layer structures, as summarized in figure 3.1(b), and thickness of the top a-Li_xSi layer increases linearly with the amount of lithiation, while thickness of intermediate c-Li_xSi layer (~800nm) was independent of lithiation capacity.

XPS depth profile, as shown in figure 3.2, indicates that the stoichiometry of Li_xSi in the top layer is $Li_{3.75}Si$, while the ratio of Li to Si varies from 3.75 to 0.5 in the intermediate layer and reaches 0.5 in the bulk unlithiated c-Si. The remained Li signal in the bulk Si was attributed to remnant from previous layers as complete removal of Li containing material through Ar ion etching is challenging. Crystallinity of each layer was characterized by EBSD, as shown in figure 3.2(b). The top layer showed no diffraction pattern, while the intermediate layer showed blurred Kikuchi pattern, indicating a strained Si lattice. The bulk unlithiated c-Si region showed a clear Kikuchi pattern attributed to (112) plane.

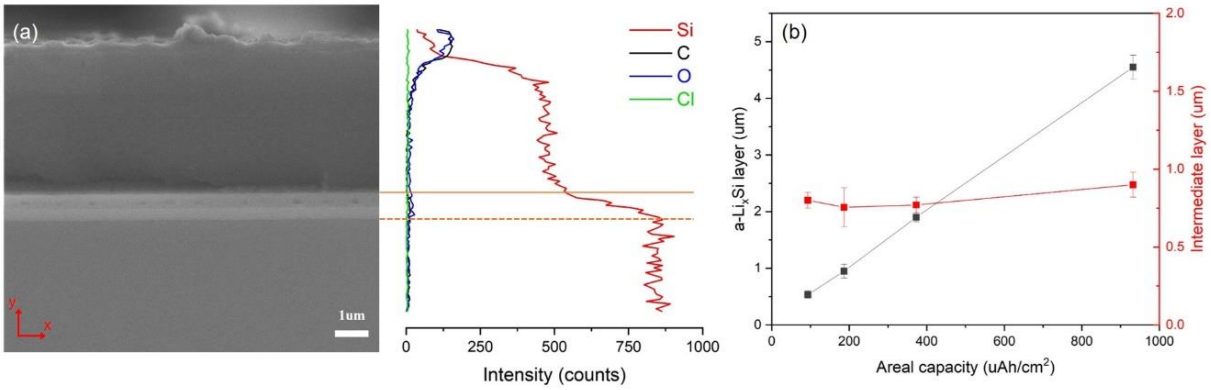

Figure 3. 1: (a) Cross sectional SEM image of lithiated single-c Si at capacity 930 uAh/cm^2 and the corresponding EDS line scan result. (b) Thickness of a-Li$_x$Si and intermediate layers at different lithaition capacity.

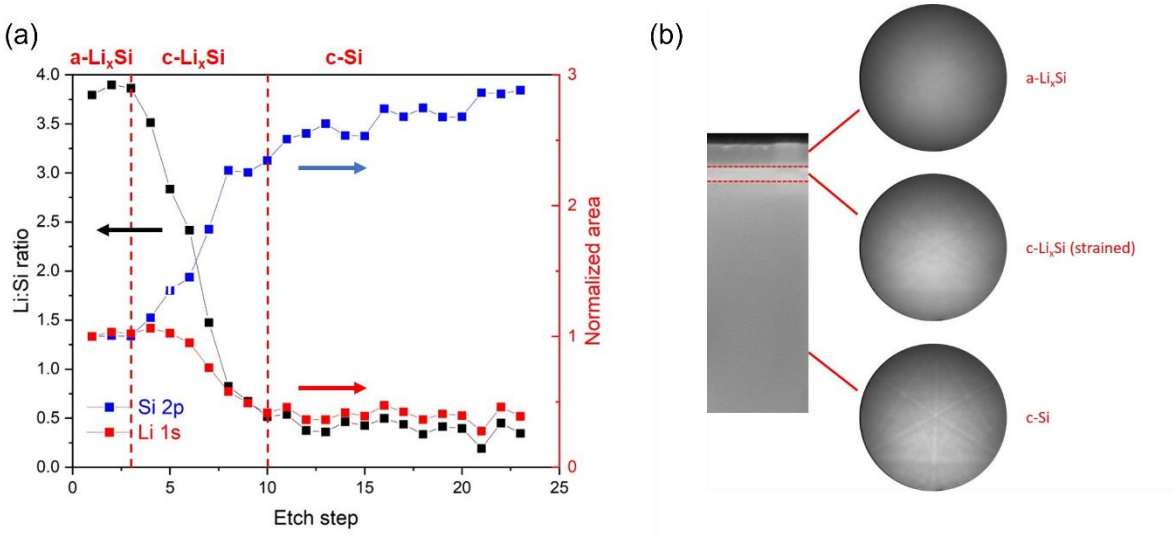

Figure 3. 2: (a) XPS depth profile of lithiated single-c Si. (b) EBSD pattern at different layers inside the lithiated single c-Si.

3.3.1.1 c-Li$_x$Si layer

The c-Li$_x$Si layer in lithiated single-c Si electrode with thickness of hundreds of nm, to the best of author's knowledge, has not been reported so far. Based on previous studies, the widely accepted view of lithiation mechanism in single-c Si is through ledge process where Si atoms peel off layer by layer, leading to two

phases in lithiated c-Si, i.e. a-Li_xSi and c-Si layers [48]. Although a similar three-layer structure has been proposed in one prior study [49], thickness of the intermediate layer between a-Li_xSi and c-Si was only ~5 nm, drastically different from the case in this study (~800nm). Comparing with prior literature, we used similar n-type doped Si electrode with similar wafer thickness [50,51]. Therefore, the difference of our result is probably due to the mechanical constraint of c-Si electrode in our electrochemical cell. As shown in figure 3.3, the single-c Si electrode in the cell was fully constrained by a SS screw at the bottom and the surface was pinned by an O-ring. Consequently, the lithiation induced stress at lithiation front exerts tensile stress on unlithated c-Si, stretching and expanding the interface to promote Li diffusion into the bulk c-Si, while for free-standing Si electrodes or Si electrodes that are clamped at one side, this tension force at phase boundary will be quickly relaxed by bending of Si substrate.

A first-order calculation can be performed to examine the change of diffusion depth due to mechanical stress; Diffusivity of solid-state diffusion is a function of stress[52]

$$D = D_0 \exp(-P\Omega/k_B T) \qquad (3.1)$$

Where D_0 is diffusion coefficient in stress-free state, P is pressure, Ω is the molar volume of Li in Si matrix, and k_BT is thermal energy. Assuming there's sufficient

Li supply at the phase boundary (3.75Li per Si), the effective diffusivity of Li can be calculated and turns out to be ~190D_0. For semi-infinite diffusion process, the characteristic diffusion length is proportional to the square root of diffusivity. So the diffusion length in the case of stress modified diffusivity is 14times higher than the case without stress. This is an order of magnitude smaller than the difference we observed (160 times difference). Therefore, if the origin of the c-Li_xSi is indeed attributed to stress enhanced solid state diffusion, then additional coupling of other physical parameters, such as Li concentration and stress gradient [52-54], must also play a role to cause this synergistic effect.

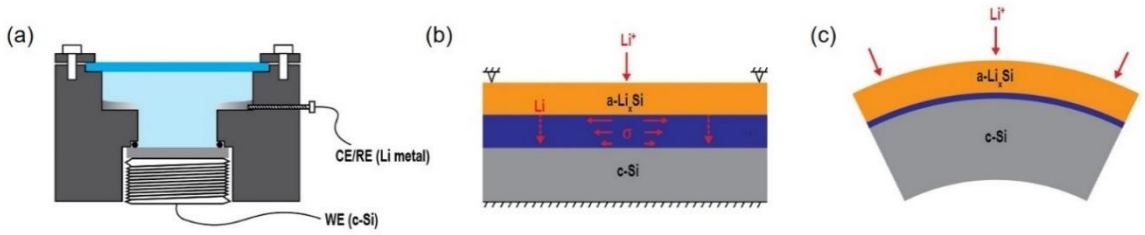

Figure 3. 3: Schematic of (a) custom-made electrochemical cell, (b) mechanical condition of c-Si electrode in the cell and layer structure of lithiated c-Si in this cell, and (c) mechanical condition of free-standing c-Si electrode and its layer structure. Note: Dashed line indicates direction of solid-state diffusion.

3.3.1.2 Stress distribution in single-c Si electrode after initial lithiation

The lithiated c-Si electrodes, after lithiation, were cleaved and mounted on an air-tight cell for Raman measurement. Raman microscope image of cross-section on cleaved Si electrode is shown in figure 3.4(a), where the phase boundary between c-

Li_xSi and bulk c-Si is clearly visible and assigned as y=0. To examine the Si Raman pattern in lithiated Si, Raman mapping was first performed, and the result showed stress variation only along thickness direction, i.e. along y-axis. Therefore, Raman line scan was performed to characterize the stress distribution across the thickness of Si electrode. The line scan ranged from bulk c-Si to the top surface of a-Li_xSi with spatial distance of 500nm, and the Raman spectra showed clear Si peaks up to 1um above the phase boundary at y=0, where Raman intensity drastically dropped in the next step, as shown in figure 3.4(b). The well-defined Si Raman peak in the region from y=0 to y=1um, as shown in figure 3.4(c), indicates crystallinity of c-Li_xSi layer, which is consistent with the previous EBSD result. Lorentzian peak was used to fit Si Raman peaks up to 1um above the phase boundary, and the fitted Raman peak position was compared with bulk c-Si (~100um below surface of Si) to obtain the Raman shift against stress-free Si. All fitted spectra showed minimal error (<1%).

Raman peak shift obtained from Lorentzian fitting is shown in figure 4 (a), and the corresponding Raman shift-stress relationship is derived in chapter 2

$$\Delta\omega = -2.3\sigma_{xx} \qquad (3.2)$$

Where $\Delta\omega$ has unit of cm^{-1}, and σ_{xx} is the uniaxial stress along x-direction with unit of GPa. From figure 3.5(a), shift of Si Raman peak to lower frequency was observed throughout the Si, which corresponds to tensile stress in Si lattice. This tensile stress increased monotonically from the bulk c-Si to the phase boundary between c-Si and

c-Li_xSi at y=0. The tensile stress reached maximum at phase boundary, and then drops. This relaxation of tensile stress can be attributed to two reasons: Plastic flow at the phase boundary, as predicted by prior theoretical work[41], and surface stress relaxation due to removal of electrochemical loading. The full width half maximum (FWHM) of Si Raman peaks is shown in figure 3.5(b), the increase of FWHM near phase boundary was not only due to Si amorphorization, but also the increased stress gradient, i.e. convolution of Si Raman peaks at different shift frequency. The magnitude of flow stress at the interface is summarized in figure 3.5(c). Comparing with previous in-situ MOSS study performed by Chon et al.[36], the magnitude of stress obtained from ex-situ Raman measurement is lower overall, while the linear trend of flow stress versus capacity is consistent. The lower stress magnitude measured by Raman spectroscopy is due to the difference of measurement setup: In our ex-situ measurement, the cross-section of Si electrodes was exposed, leading to removal of stress in the out of plane direction, and therefore, the measured stress is a uniaxial stress along x-direction. In the in-situ MOSS measurement, however, a biaxial stress in the plane normal to thickness direction was measured.

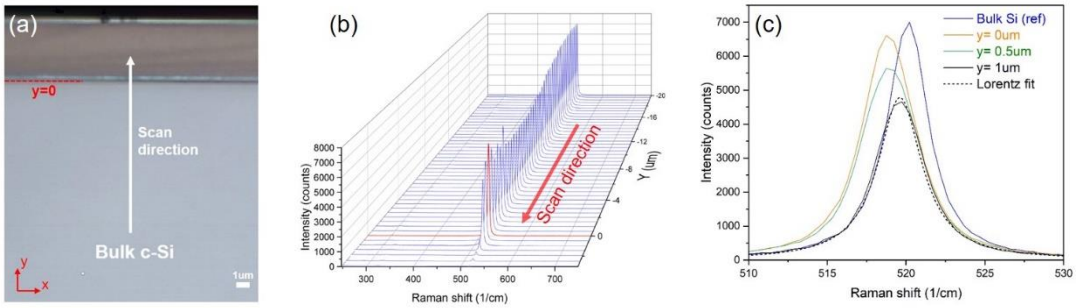

Figure 3. 4: (a) Raman microscope image of cross-section of lithiated c-Si at 930uAh/cm^2. (b) Raman spectra obtained from line scan. (c) Si Raman peak shift near phase boundary and the corresponding Lorentzian peak fitting.

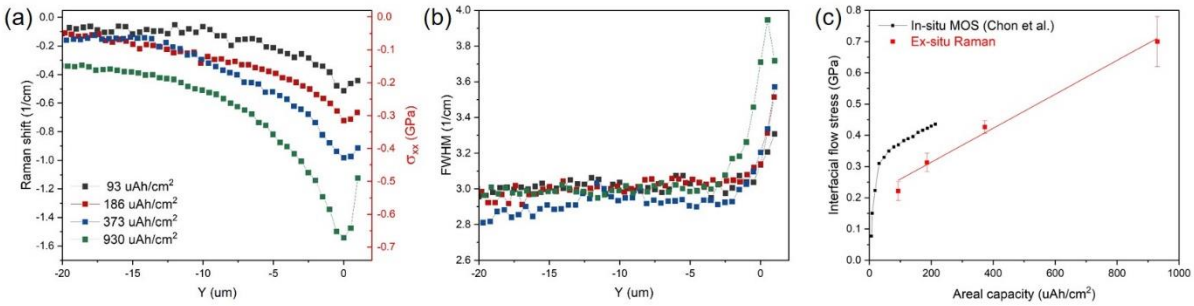

Figure 3. 5: (a) Si Raman peak shift obtained from line scan with the calculated uniaxial stress, and (b) the corresponding FWHM of Si Raman peak. (c) Flow stress at phase boundary with different lithiation capacity.

3.3.2 Single c-Si electrodes after initial delithiation

Single-c Si electrodes after initial delithiation were also investigated. Electrode samples with two different delithiation conditions were prepared: The first sample was lithiated to 93 uAh/cm^2 and then delithiated to 1.4V, while the second sample was lithiated to 186uAh/cm^2 and delithiated to 1.4V. The GV charge/discharge curves are shown in figure 3.6(a). Based on the cross-sectional SEM images, as shown in figure 3.6(b), the first sample didn't crack after initial delithiation, and

thickness of a-Li_xSi layer was largely reduced, down to tens of nm, while c-Li_xSi layer thickness reduced to ~250nm. In addition, the previous clear phase boundary between c-Li_xSi and c-Si smeared out after the initial delithiation step. Raman mapping on the cross section shows compressive stress near the surface, with the majority of bulk c-Si went into stress neutral state, as shown in figure 3.6(c). The compressive stress in single-c Si electrode is an obvious consequence of plastic flow at phase boundary during lithiation process, since in the case of elastic deformation, the delithiation process can only relax the tension in Si electrode, instead of leading to compressive stress. For the second sample, crack formation was captured in the SEM image, as shown in figure 3.7(a). Additionally, the cross-sectional SEM image shown in figure 3.7(b) indicates that thickness of both a-Li_xSi (~400nm) and c-Li_xSi (~400nm) layers in the second sample weren't reduced significantly. The crack initiated in the middle of the delithiation process and deflected along the phase boundary between c-Li_xSi and c-Si, exposing the underlying c-Si layer, which then caused delithiation step to end prematurely. Cross-sectional Raman mapping also shows highly localized stress pattern, as shown in figure 3.7(c), with some area in compressive stress state (corresponding to the complete local delithiation) some area in tensile stress (corresponding to incomplete local delithitation, i.e. Li trapped inside Li_xSi due to premature ending of delithiation process) and some area shows

neutral stress state (corresponding to de-cohesion of Li_xSi from c-Si substrate). The Raman stress pattern is consistent with the conclusion obtained from SEM result.

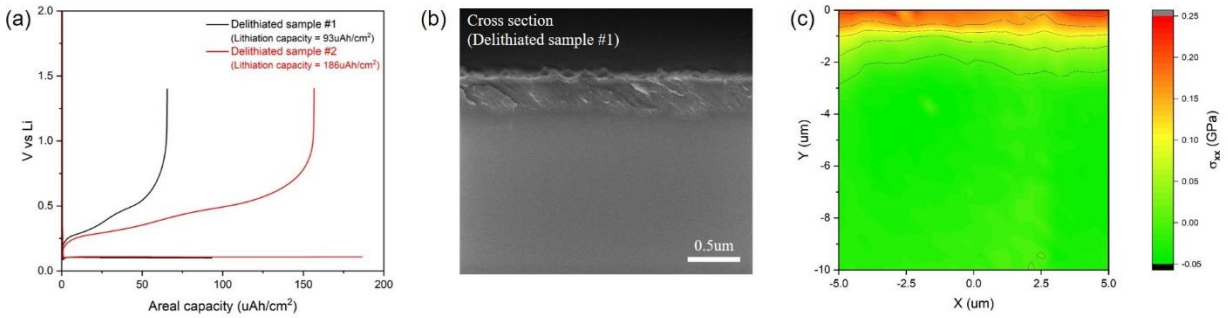

Figure 3. 6: (a) GCD curves of c-Si electrodes at different cycle conditions. (b) Cross-sectional SEM image of delithiated c-Si with initial Li loading 93uAh/cm^2. (c) Raman stress mapping of the same c-Si electrode after initial delithiation.

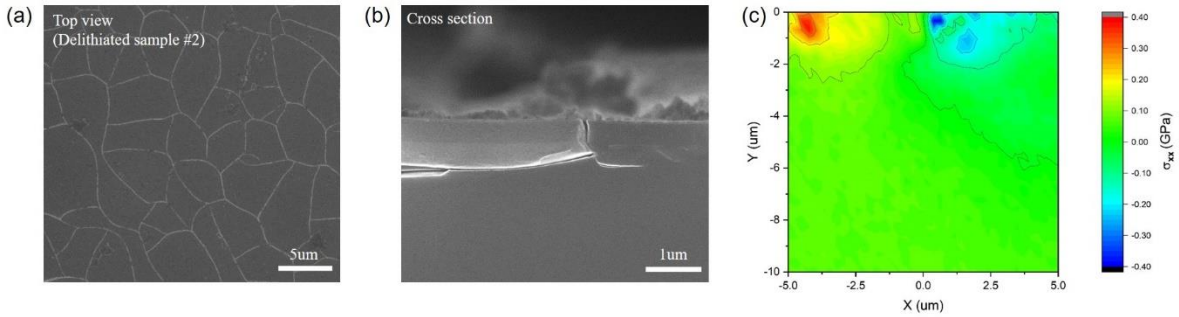

Figure 3. 7: (a) Top view SEM image, and (b) Cross sectional SEM image of delithiated c-Si with initial Li loading 186uAh/cm^2. (c) Raman stress mapping of c-Si with same delithiation condition.

3.3.3 Cycled single c-Si electrodes

Extended cycling was performed on the sample with initial lithiation capcity of 93uAh/cm^2, to examine the mode of crack initiation and electrode damage. During the cycling experiment, the c-Si electrode was lithiated to 93uAh/cm^2 at each discharge step, and then delithiated to 1.4V in the following charge step. GV cycling

curve is shown in figure 3.8(a). In the first five cycles, the columbic efficiency dropped monotonically, from 70 to 17%. The initially higher columbic efficiency is due to facile Li extraction from unstable SEI layer. As the SEI layer stabilized in the following cycles, the sluggish delithiation kinetics in Li_xSi started to take over, leading to lower columbic efficiency. From 5th to 10th cycle, however, the columbic efficiency increased back up again due to crack formation, which exposed fresh Si for additional SEI layer formation. The SEM image of sample at the 4th cycle is shown in figure 3.8(b), where no visible crack formation was observed, and image of sample at 10th cycle is shown figure 3.9(a), where cracks on the surface are readily observed. However, cross-sectional SEM images shown in figure 3.9(b) and 3.9(c) indicate that the cracks only grew in the direction along thickness, without any lateral deflection as seen in previous delithiated sample #2. In addition, these vertical cracks expanded in the following cycles without delamination.

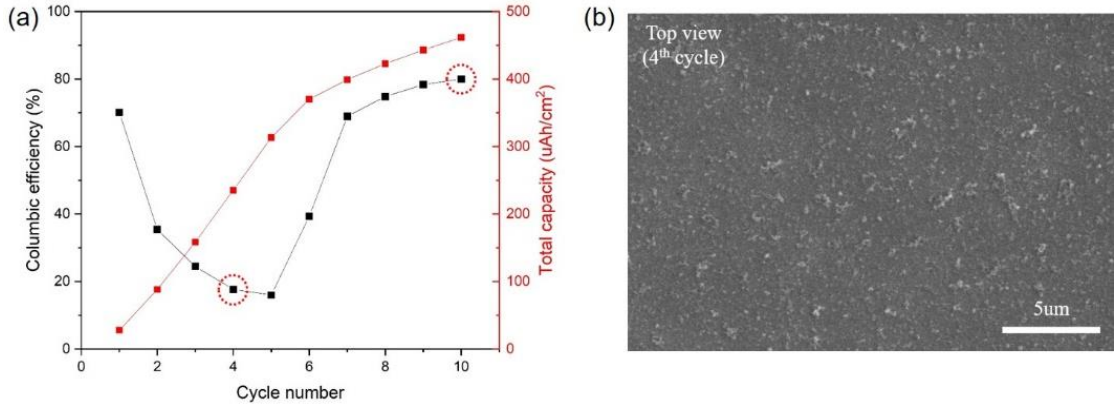

Figure 3. 8: (a) Columbic efficiency and total capacity of c-Si electrode in the end of each delithiation cycle. (b) Top view SEM image of c-Si electrode after the 4th cycle.

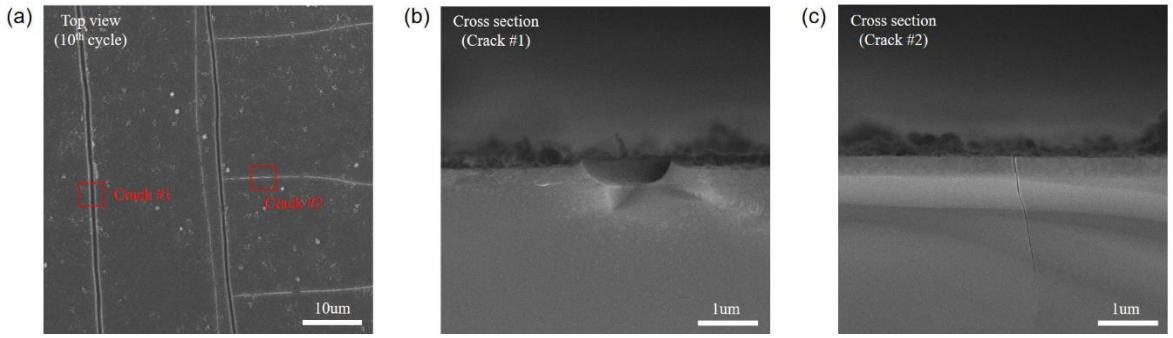

Figure 3. 9: SEM images of (a) top surface of c-Si electrode after the 10th charge/discharge cycle, (b) cross section of crack that forms at early cycle, and (c) cross section of crack that forms at later cycle.

3.3.4 Failure mechanism of single c-Si electrodes

Crack initiation and propagation in single-c Si electrodes showed different pattern as cycling condition changes. Based on the SEM and Raman results, we propose a model for failure mechanism in c-Si, as summarized in figure 3.10: For single-c Si with low initial lithiation capacity (i.e. 93uAh/cm2), cracking does not occur in the following delithiation process, as there is not enough stress gradient

along the thickness direction to rupture Si electrode. In the next few cycles, more Li ions are trapped inside Si due to sluggish delithiation kinetics of c-LixSi, leading to thicker c-Li_xSi layer and larger stress gradient. After certain number of cycles (in our case, 6th cycle), the stress gradient reaches a critical level to initiate crack formation, which then propagates and expands in the following cycles without causing any delamination of Si. For single-c Si with high initial lithiation loading (i.e. 186uAh/cm^2), the flow stress at the phase boundary is higher, which then lead to high stress gradient in Li_xSi in the following delithiation cycle. Cracks then initiate in the middle of the delithaition process, and due to high stress release rate accompanied with high stress gradient, the crack propagates not only across the thickness of Li_xSi, but also deflects along the phase boundary between c-Li_xSi and c-Si, leading to exposure of fresh unlithiated c-Si. Consequently, delithaition process ends prematurely without significant removal of Li from both c-Li_xSi and a-Li_xSi layers.

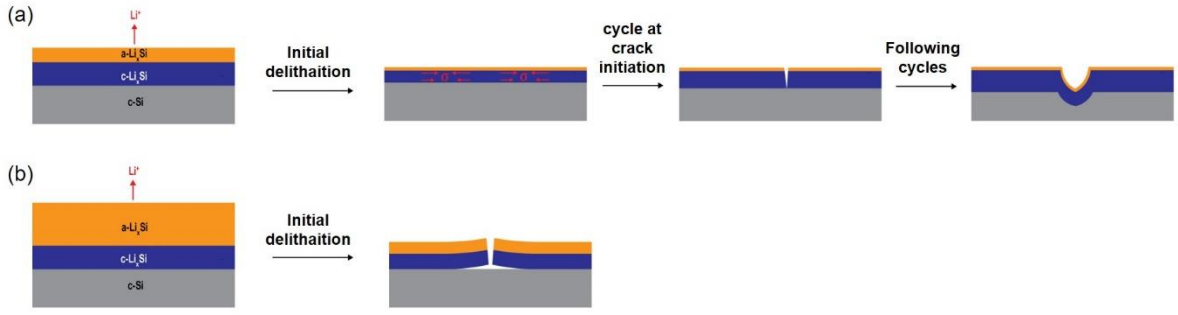

Figure 3. 10: Schematic of failure mechanism of (a) single-c Si electrode with low initial Li loading, and (b) single-c Si electrode with high initial Li loading.

3.4 Conclusion

In this chater, we investigated stress distribution and crack formation in single-c Si electrodes. For lithiated Si electrodes, a surprising three-layer structure was found, and its origin was attributed to the mechanical constraint in our electrochemical cell and ECM coupling in single-c Si electrodes. Stress distribution in the electrodes was characterized by ex-situ Raman measurement, and plastic flow at phase boundary after initial lithiation was found. The magnitude of flow stress at the phase boundary showed a linear correlation with lithiation capacity, which is consistent with prior literature. For single-c Si electrodes after initial delithiation, the electrodes with high initial loading cracked readily during the initial delithaition step, and the cracks propagated along Si thickness direction and deflected along the phase boundary. For Si electrodes with lower initial loading, however, cracks didn't initiate until further cycling, and unlike the case with high Li loading, cracking only initiated and propagated along Si thickness. A model for crack initiation and propagation in single-c Si electrodes was proposed based on the SEM and Raman results. Our work demonstrates a detailed stress study in single-c Si electrodes using Raman spectroscopy, which is currently lacking in the literature.

Chapter 4: In-situ stress characterization of patterned poly-crystalline Si thin film electrodes

4.1 Introduction

Si electrode is known for its large volume change during Li insertion/extraction. As a consequence, the mechanical failure of Si electrodes after a few electrochemical cycles, such as cracking and pulverization, greatly limits its application in Li-ion batteries. Si nanoparticles, however, have shown excellent mechanical durability[55]. The small size leads to confined strain energy in Si nanoparticles, which enables Si electrode to maintain the structural integrity over extensive electrochemical cycles. Si thin films, on the other hand, have also shown improved mechanical performance compared to its bulk counterpart, and it has been experimentally observed that critical size of Si thin film, both thickness and width, exist[56-59]. Below the critical values, Si thin film electrodes don't undergo cracking or other mechanical failure. For both small form Si electrodes, it has been predicted that ECM interaction plays a critical role on its outstanding mechanical performance.

Understanding of ECM interaction in nano-sized Si electrodes and Si thin films is currently governed by theoretical studies [60-63], with only handful of experimental studies exist. The challenge of experimental study in this length scale is that Si particles and patterned Si thin films have exposed edges, which induces certain stress

relaxation and gradient across the electrodes. Thus, experimental study of ECM effect requires characterization techniques that has scanning capability so a stress distribution from core to the edge of Si electrodes can be resolved. For traditional stress characterization techniques such as MOS, only average stress variation can be detected and thus, become unsuitable for detailed stress characterization in those small form Si electrodes. Raman spectroscopy, however, when it's coupled with microscope and confocal apertures, can provide sub-micro scanning resolution for detailed stress study in the crystalline electrodes. However, combining Raman spectroscopy with in-situ stress characterization in liquid electrochemical cell requires extra care [64,65]. A matched refractive index of medium between objective lens and sample surface must be taken care in order to fully utilize the scanning resolution of u-Raman. Unfortunately, to the best of author's knowledge, this kind of work is still lacking in literature.

In this chapter, we demonstrate an in-situ Raman study of pattered Si thin film electrodes. A novel electrochemical cell was designed and fabricated to combine with the u-Raman spectroscopy. The experimental setup showed a scanning resolution down to ~500nm. Patterned poly-c Si thin films with square shapes were fabricated through photolithography and two different sizes of squares were studied. Tungsten thin film was selected as current collector due to its process compatibility with poly-c Si deposition and etching, but tungsten oxide formed at elevated

temperature during LPCVD process and undesired electrochemical reaction was observed during cycling. By controlling the potential range in electrochemical experiments, we conditioned the tungsten oxide layer, and in the following cycles, we successfully excluded the parasitic reaction from tungsten oxide and characterized the stress distribution in poly-c Si electrodes. Different profile of stress distribution was observed for different sizes of Si square electrodes, and FEM modeling was used to explain the difference of stress distribution between patterned poly-c Si electrodes. A comprehensive understanding of ECM coupling effect in Si thin film electrodes was obtained from this study and it showed a good consistency with prior literature.

4.2 Experimental

4.2.1 Sample fabrication

The fabrication process for patterned poly-c Si thin film electrodes consists of four steps: First, 500nm of SiO_2 was grown on 3in wafers through thermal oxidation. Second, 100nm of tungsten thin film was deposited through sputtering process at room temperature. Third, Poly-c Si thin film was deposited on the substrate through LPCVD process at 650^{o}C and patterned into different size of squares through photolithography and RIE processes. Lastly, the samples were sonicated in acetone

solution to remove residual photoresists and a short dip in buffered oxide etchant solution to clean the surface.

4.2.2 μ-Raman spectroscopy

During Raman measurement, a 60X water immersion objective lens with NA0.95 was used (Olympus, LUMPlanFl). 633nm laser (HeNe) with D1 intensity filter were used, and the incident laser power was controlled to 1mW. 400um hole and 100um slit were used and for each acquisition, and 8s exposure was chosen to maintain a balance between Raman signal intensity and destruction to lithiated poly-c Si electrode.

4.2.3 X-ray diffraction (XRD)

As-fabricated samples without patterning were characterized by powder XRD. Diffraction patterns were measured using CuKα radiation in Bragg–Brentano geometry. Bruker D8 Advance powder diffractometer (Karlsruhe, Germany) equipped with theta-theta goniometer and LynxEye position sensitive detector was used. Data were collected from 10 to 65° 2θ with step size of 0.015° and counting time of 2 s per step. ICDD powder diffraction database was used for XRD spectra matching.

4.3 Results and discussion

4.3.1 patterned poly-c Si thin film electrodes

Fabrication of patterned poly-c Si thin film electrodes is elaborated in section 4.2.1, and process flow is shown in figure 4.1(a). As fabricated Poly-c Si thin film electrodes were examined by SEM, as shown in figure 4.1 (b) to (d). Based on figure 4.1(b) and (c), the square shaped poly-c Si islands were patterned with high spatial resolution. Thickness of each layer was also characterized by cross-sectional SEM, as shown in figure 1(d), where thickness of tungsten was 100nm, and poly-Si was 200nm. In addition, edge of the patterned poly-c Si was straight, indicating a good directionality of RIE etch.

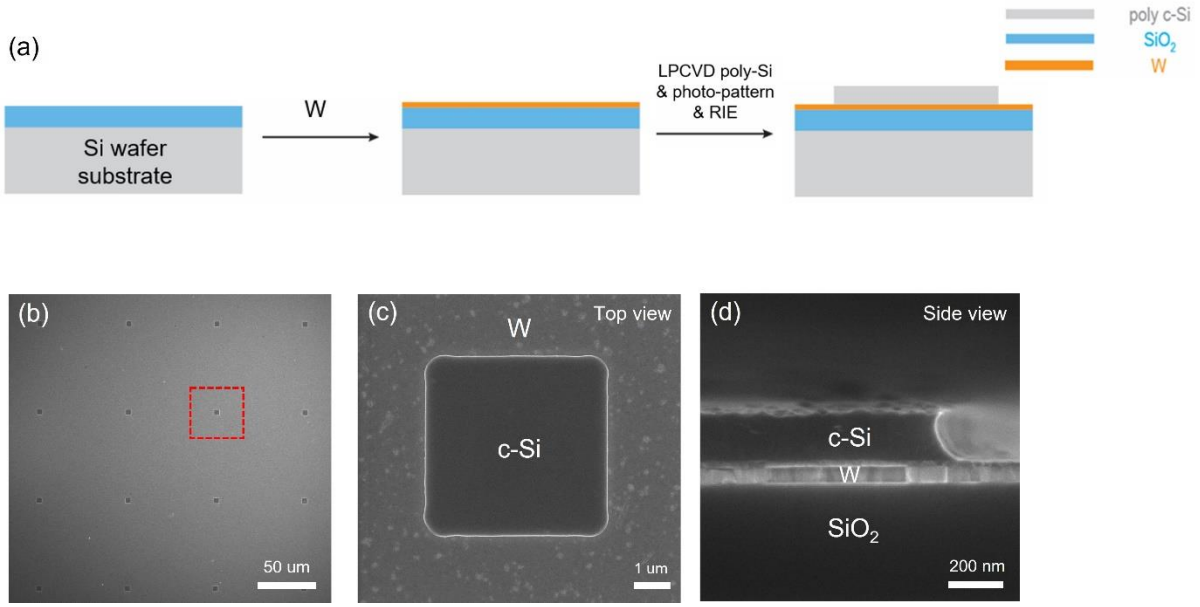

Figure 4. 1: (a) Schematic of fabrication process of Si thin film electrodes. Top view SEM images of as-fabricated Si thin film electrodes in (a) low magnification, and (b) high magnification (image area corresponds to red dashed square in (b)). (d) Cross-sectional SEM image of as-fabricated Si electrodes.

4.3.2 In-situ Raman setup and critical measurement condition

A custom-made in-situ Raman cell, as shown in figure 2 (a), was used throughout this study, and design details of this cell was elaborated in chapter 2. In order to avoid optical aberration and improve confocality, a 60X water immersion objective lens with NA=0.95 was used. The schematic of operation of in-situ Raman experiment is shown in figure 4.2(a), and a picture of the in-situ Raman experiment setup is shown in figure 4.2(b). During in-situ measurement, one of the challenges in SEI layer formation on the surface of lithiated Si electrode, which blocks the laser beam access to the Si layer. In addition, laser over-exposure can induce parasitic electrochemical reaction at the surface of Si, as shown in figure (c). The white sphere

presented on the surface of Si-island was induced under 3mW laser exposure for 5 second. This product didn't re-dissolve in delithiation process and could not be removed by dimethyl carbonate solution. In short, careful selections of lithiation potential and laser exposure power need to be considered, in order to maintain a good Raman signal and avoid damage on surface the lithiated Si. In this study, we found that 1mW laser power and exposure of 8 second give a good combination of Raman intensity and surface integrity of lithiated Si.

Spatial resolution of in-situ Raman setup was first tested by a line scan on patterned poly-c Si electrode. The microscope image of a patterned Si square is shown in figure 4.3(a). For 5um wide poly-c Si electrode, Raman line scan with 0.5um step size, as shown in figure 4.3(b), indicated a good confocality of this in-situ setup: outside Si electrode region, Si peak intensity substainly dropped. A typical Raman spectrum of lithiated poly-c Si electrode at 0.15V vs Li^+/Li is shown in figure 4.3(c), where three peaks were observed. The peak at ~450 cm^{-1} is attributed to ClO_4^- ion in polycarbonate solution [66], as this peak was also observed outside the Si electrode region. The peak at ~510 cm^{-1} is attributed to nanocrystalline Si particles and the peak at ~520 cm^{-1} is attributed to bulk c-Si.

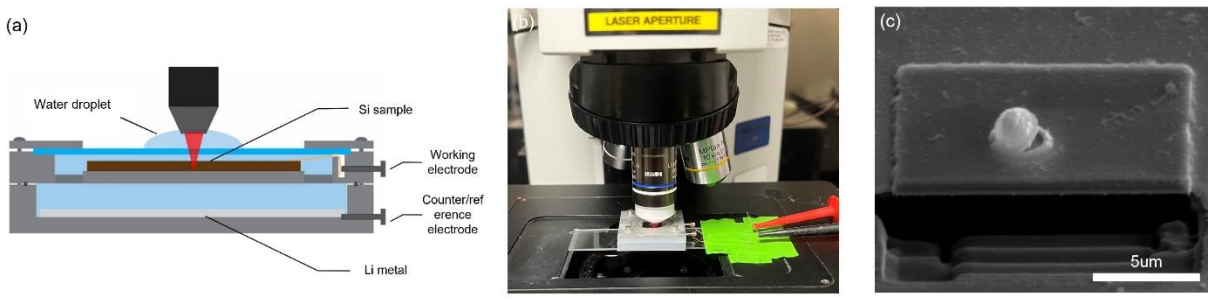

Figure 4. 2: (a) Schematic of in-situ Raman measurement. (b) Picture of in-situ Raman experiment. (c) SEM side view image of poly-Si electrode lithiated at 0.15V, the white sphere is formed after 3mW laser exposure for 5seconds (FIB cutting was applied at the edge).

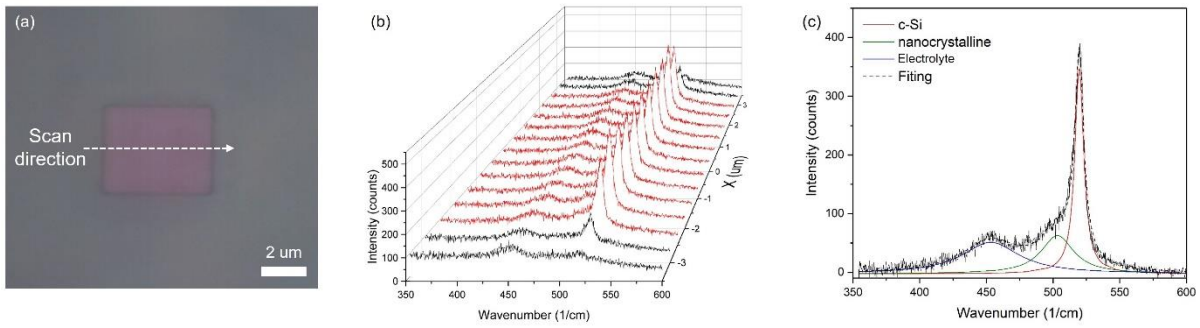

Figure 4. 3: (a) Microsope image of Si square island with 5um width. (b) Raman spectra obtained from line scan of the Si square in (a). (c) Typical Raman spectrum of lithiated Si and peak fitting.

4.3.3 Tungsten oxide formation and substrate conditioning

Poly-c Si electrode was deposited through LPCVD process at 650^{o}C, where silane gas decomposes at elevated temperature. Tungsten current collector was chosen in this study because it has high thermal stability, and tungsten silicide forms at temperature above 650^{o}C [67,68], so it's compatible with the LPCVD process. The Si substrate with tungsten thin film before and after poly-c Si deposition were characterized by XRD, as shown in figure 4.4(a). The sputtered tungsten thin film

showed a strong diffraction peak at $2\theta \approx 40^o$, corresponding to (110) plane of α-W, while a minor peak at $2\theta \approx 35^o$ deg also presented, attributed to the beta phase of W. Poly-c Si thin film sample showed strong diffraction peak at $2\theta \approx 47^o$, which corresponds to (220) plane, indicating that the majority of poly-c Si was along the [110] direction. Thus, in the following Raman stress analysis, stress calculation was based on assumption of [110] Si. Presence of tungsten oxide was also observed, with a diffraction peak observed at $2\theta \approx 24^o$.

In the electrochemistry characterization, presence of tungsten oxide was also observed. In a CV study with potential range from 0.01V to 1.4V, as shown in figure 4.4(b), redox peaks of tungsten oxide appeared in the potential range between 0.8V and 1.1V. Tungsten oxide lithiation at this voltage range goes through conversion reaction, which generates a large volume expansion [69,70]. Therefore, it is crucial to exclude the redox reactions of tungsten oxide during the in-situ Raman stress characterization in poly-c Si electrode.

Since the potential range of redox reactions is different for tungsten oxide (0.8-1.1V) and Si (0.05-0.6V), we selectively lithiated the tungsten oxide layer by sweeping the potential to 0.3V at the initial electrochemical cycle and the potential was held for 2 hours. Then, the potential swept back to 0.8V to finish the substrate conditioning. As shown in figure 4.5, Raman mapping at a few different potentials was conducted to characterize the stress state of poly-c Si during the substrate

conditioning. At open circuit potential (OCV), small stress gradient (0.1GPa) was observed across poly-c Si electrode. This is caused by lattice mismatch between W and Si layer. As cell potential reaches 0.4V vs Li^+/Li, the stress gradient from the edge of poly-c Si island to the core dramatically increased. The tensile stress near the edge of Si electrode was induced by expansion of lithiated tungsten oxide, while the compressive stress in the center of Si was likely attributed to the bending of Si film since at this stage, Li distribution in tungsten oxide layer was probably not uniform, leading to a higher altitude at the edge and lower at the center in the poly-c Si electrode. Additionally, corners in poly-c electrode showed the highest tensile stress, which is probably due to higher local Li concentration (i.e. larger Li flux at corners due to larger local area). At 0.3V, the stress distribution evolved into a more uniform pattern, as lithium distribution in tungsten oxide substrate became more uniform. In the course of potential sweeping back to 0.8V, linear I-V curve was observed, indicating the absence of electrochemical reactions in this potential range. Correspondingly, the stress distribution pattern at 0.8V showed a very close similarity to stress pattern at 0.3V, except that the tensile stress at corners was eased. This implies that tungsten oxide layer reached a uniformly stretched stress condition.

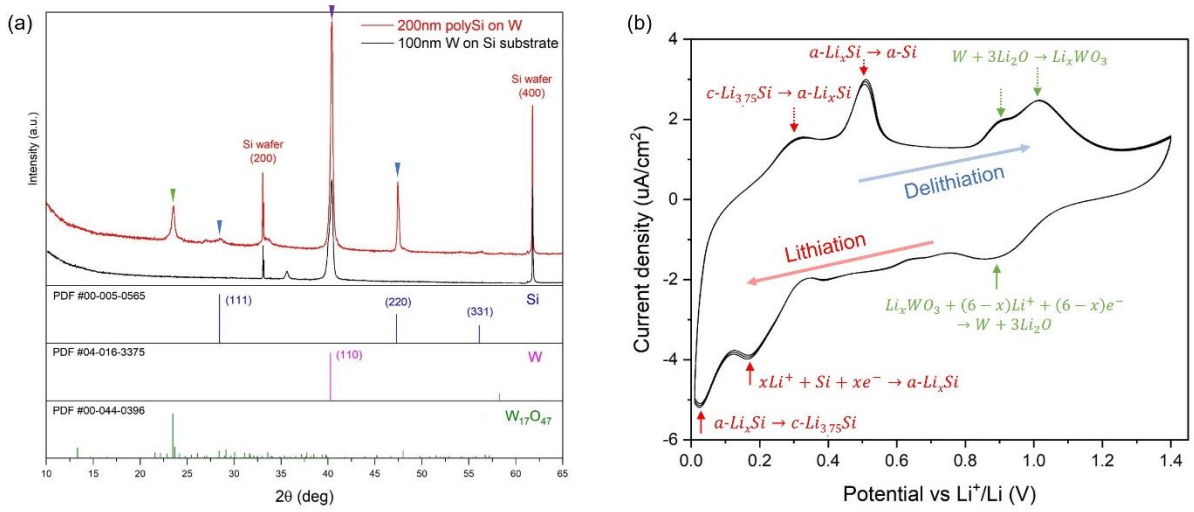

Figure 4. 4: (a)XRD pattern of poly-c Si on W and blanket W thin film on Si wafer substrate. (b) CV curve of poly-c Si device at potential range between 10mV and 1.4V.

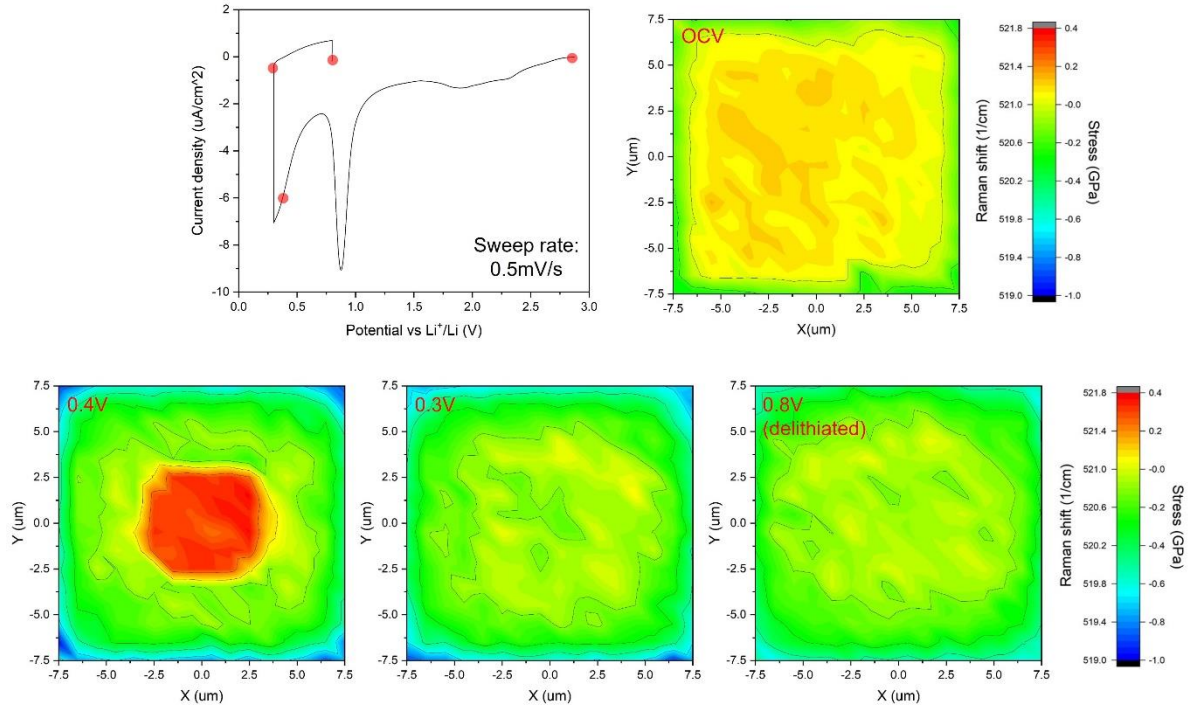

Figure 4. 5: I-V curve during substrate conditioning in the initial cycle and Raman mapping of poly-c Si device at different potential.

4.3.4 Stress condition of Si during lithiation/delithiation

After substrate conditioning, the cell was then cycled between 0.15V and 0.8V to lithiate/delithiate poly-c Si layer. For better quantitative analysis and capturing kinetic response of poly-c Si, Raman line scan, instead of mapping, was performed at different potentials, and the CV curve is shown in figure 4.6 (a). Raman line scan results for poly-c Si squares with width of 5um and 15um are shown in figure 4.6 (b) and (c). For 5um square, the poly-c Si layer first underwent transition from stress neutral state to tensile stress state after substrate conditioning. The tensile stress induced by lithiated tungsten oxide layer was ~0.7GPa, and the stress distribution in poly-c Si layer was uniform. At 0.2V, lithiation of Si readily started, which induced tensile stress in poly-c Si. This tensile stress balanced the tensile stress imposed by lithiated tungsten oxide layer, which relaxed the overall stress condition in poly-c Si. At higher lithiation potential of 0.15V, the tensile stress continued to drop, while it dropped faster in the center region than the edge, forming a dome shaped stress profile. This indicates that lithiation occurred preferentially at the center than the edge. In the following delithaition process, stress in poly-c Si moved back into a tensile state as Li was continuously extracted, and interestingly, at the highest delithiation state at 0.8V, magnitude of tensile stress was even higher than the tensile stress at starting potential.

For poly-c Si square with 15um width, similar trend of stress pattern shifting occurred after substrate conditioning. After lithiation occured at 0.2V and 0.15V, tensile stress in poly-c Si was relaxed as lithation induced tensile stress balanced the tensile stress imposed by tungsten oxide substrate, while in this case, a strong stress gradient near the edge was observed. Additionally, tensile stress reached a local maximum at ~2.5um away from the edge and seemingly formed a plateau in the center region. During delithiation, the overall stress state moved back to higher tensile condition, but instead of moving to higher tensile state, the magnitude of tensile stress was at similar level as the original point. The difference of stress shifting behavior at the end of charging process (i.e. at 0.8V) between two different poly-c Si electrodes is probably attributed to inconsistent resistivity of current collector (lithiated W oxide became thicker and higher resistance), which leads to different overpotential in poly-c Si electrodes.

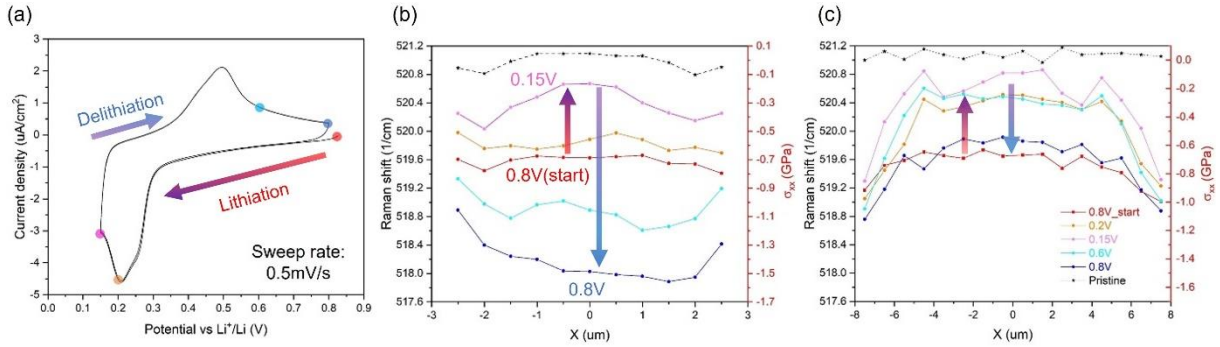

Figure 4. 6: (a) CV curve of poly-c Si electrode at 2nd cycle (I.e. after initial substrate conditioning). (b) Raman line scan of patterned poly-c Si electrodes with (b) 5um width, and (c) 15um width.

4.3.5 ECM modeling and critical size effect in patterned Si electrode

FEM modeling with ECM coupled physics was used to explain the stress distribution in patterned poly-c Si electrodes. Formulation of this model is elaborated in chapter 2, and the boundary conditions are shown in figure 4.7. In this model, 2D geometry was used to represent the cross-section of patterned poly-c electrode, with assumption of plain strain condition. Electrical potential with sweeping rate of 0.5mV/s was applied to the top surface of Si electrode and the bottom side of Si electrode was mechanically constrained along the y-axis, while extension along the x-axis is allowed. It should be noted that the boundary condition exhibited here does not accurately reflect the case in experiment, the goal here is to investigate the nominal stress in poly-c Si (unlithiated layer) induced by lithaited Si (lithiated layer) and compare the trend between modeling and experiment, instead of matching the values precisely.

Modeling result of Li concentration along with deformed geometry of poly-c Si electrode after lithiation and delithiation are shown in figure 4.8(a) and (b). At lithiation potential of 0.15V, a Li concentration gradient was built up along the thickness direction in Si electrode, due to sluggish Li diffusion kinetics. As a result, the top surface of Si electrode stretched more extensively than the bottom, leading to a dome shape deformed geometry. At delithiation potential of 0.8V, the Li concentration gradient was inverted, again, due to sluggish Li diffusion kinetics, and some Li was trapped inside Si electrode without being completely depleted. In this case, the inverted Li concentration gradient led to bowing of Si electrode. For both lithiated and delithiated state, maximum Li concentration occurred at corners in Si electrode, which is attributed to mechanically enhanced and impeded diffusion process, demonstrating ECM coupling effect in Si electrode.

In this model, Si electrodes with two different widths, 0.5um and 5um, were studied, and to compare the stress value obtained from modeling with experimental results, it was assumed that the top 100nm on the surface of Si electrode became amorphous during lithiation, and thus didn’t contribute to the Raman peak shift. Therefore, the average stress value in the bottom 100nm of Si electrode was calculated and shown in figure 4.8(c) and (d). For 0.5um wide Si electrode, a parabolic tensile stress profile was observed at lithiation potential of 0.15V. The higher tensile stress at the center of Si electrode was attributed to lithiation induced

expansion, while near the edge of Si electrode, the tensile stress was relaxed due to higher degree of freedom. At delithated state, the stress pattern was inverted into compressive state, as an inverted Li concentration gradient was developed, which caused compression on the bottom Si. The stress pattern of 0.5um wide Si electrode matches closely with the experimental result obtained from 5um wide Si electrode.

For 5um wide Si electrode in the model, stress distribution showed a different profile: a stable stress plateau in the center region of Si electrode occurred, while a stress gradient was developed near the edge. Similar stress inversion behavior was also observed after the Si electrode was delithiated at 0.8V. The model results here resemble the experimental result for 15um wide Si electrode, except that in experiment, a revered stress profile after delithiation was not observed.

The difference of stress profile between different size of poly-c Si electrode has previously been explained by a pure mechanical “shear lag” model in another work [59], while in our case, we used a fully coupled ECM model to arrive at the same conclusion. In addition, the ECM modeling results here have an important indication of the critical size effect in patterned Si electrodes: When the width of patterned Si electrode is below the critical size, the lithiation/delithiation induced stress can be fully relaxed by edge expansion and rotation, as shown in figure 4.8(a). While for Si electrode above the critical size, the lithiation/delithiation induced stress in the center region cannot be relaxed by edge expansion and rotation, instead, shearing against

the substrate becomes the dominating stress relaxation mode, leading to a stress plateau in the stress distribution profile, as indicated in figure 4.8(d). When the shearing stress is large enough, decohesion of Si from the current collector substrate can occur, which leads to increased electrode resistance and capacity fading when the Si thin film electrode is applied in LIB system. This conclusion is consistent with prior experimental study where patterned Si electrodes below certain size became much more mechanically endurance and can last over hundreds of cycles without cracking or delamination[58,59]. It's also worth noticing that the deformed shape of Si electrode obtained from modeling resembled well with experimental observation from another work[71], which further validates our model result and understanding of ECM effect in patterned poly-c Si electrodes.

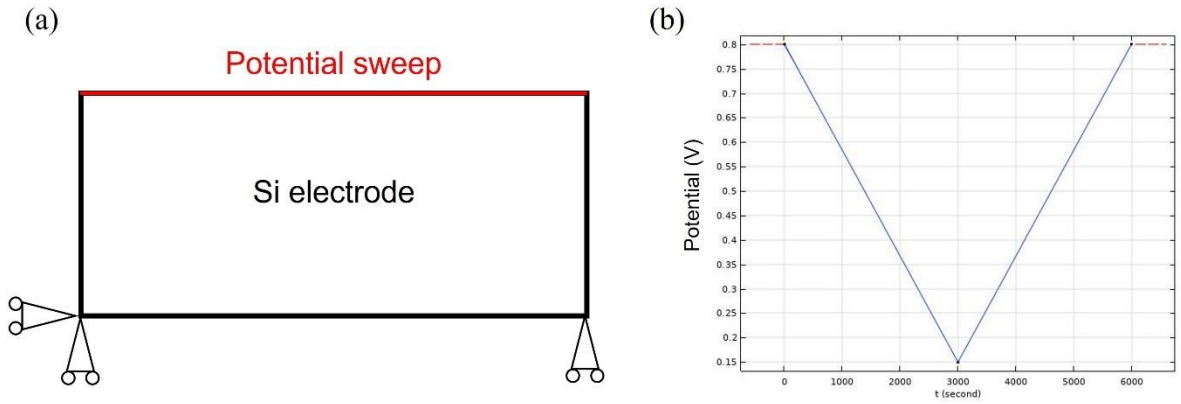

Figure 4. 7: Schematic of (a) geometry and boundary condition of the ECM model, and (b) electrical potential applied to the surface of Si electrode as a function of time.

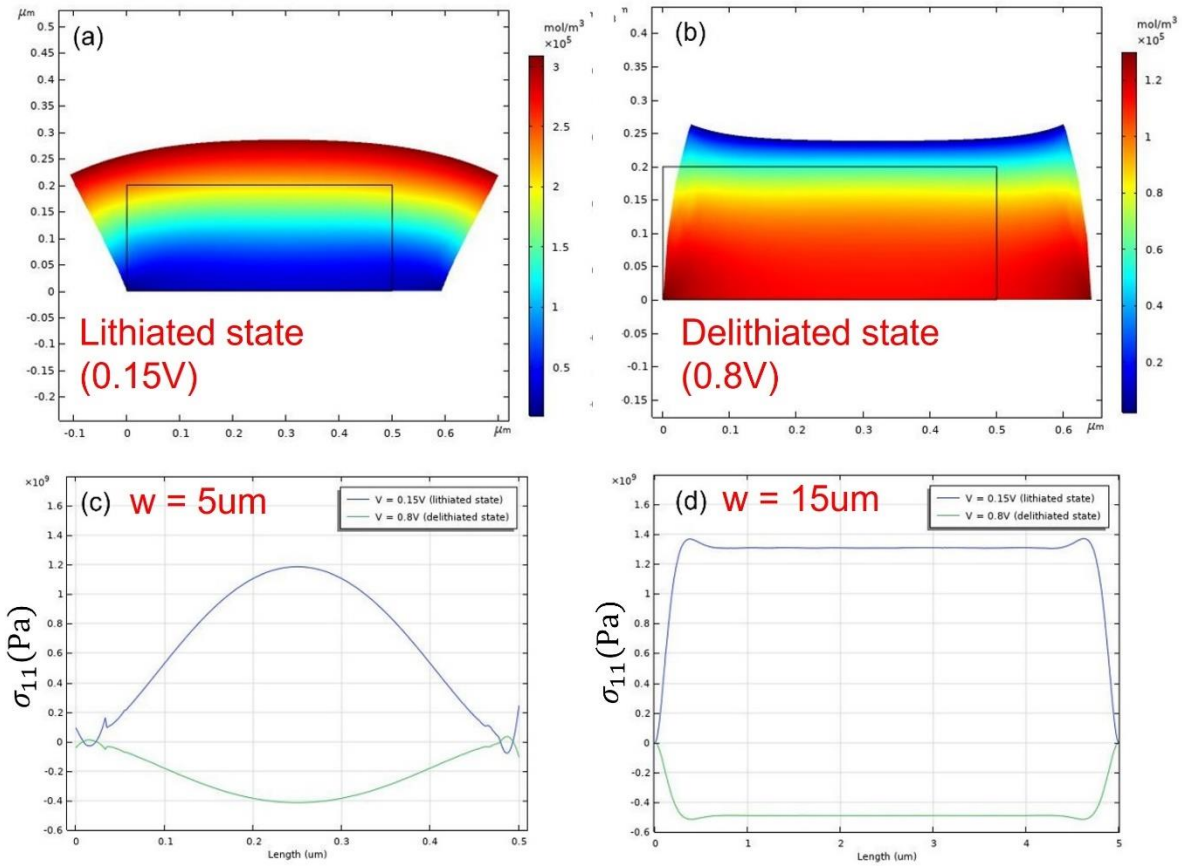

Figure 4. 8: Fig 4.8 Modeling result of deformed geometries and Li concentration distribution in Si electrode at (a) 0.15V, and (b) 0.8V. Modeled lateral stress distribution in Si electrode with (c) 5um width, and (d) 15um width.

4.4 Conclusion

In this work, we demonstrated a novel in-situ Raman experiment setup for stress characterization in patterned poly-c Si thin film electrodes. The experimental setup showed high scanning resolution, which enabled a detailed stress study in patterned Si electrode. W was selected as current collector due its high thermal stability and process compatibility with LPCVD deposition of poly-c Si. However, tungsten oxide formed during LPCVD process, which caused undesired electrochemical reaction in

our experiment. By controlling the potential range of CV in the initial cylce, we conditioned the tungsten oxide layer to obtain a uniformly stretched substrate for later stress measurement on poly-c Si electrode. In the following CV cycles, we measured the dynamic stress change in Si at different potentials. Patterned poly-c Si electrodes with two different sizes, 5um and 15um, were studied, and different stress distribution profile of those electrodes indicated different stress relaxation modes. By using FEM modeling, we were able to understand the origin of different stress profile in patterned Si electrodes. A comprehensive picture of ECM coupling was obtained and showed a good consistency with prior studies.

Chapter 5: Stress characterization in solid-state-battery platform

5.1 Introduction

Solid state batteries (SSBs) have been regarded as the next generation battery system. Due to the employment of solid electrolytes that have wide electrochemical stability window [72-74], SSBs can be coupled with high energy density electrodes such as Li metal. As a result, SSBs can have much higher energy density than its liquid counterparts. Also, the inorganic solid electrolytes are not flammable, which enables higher safety of SSBs.

However, development of SSBs is still facing challenges from compatibility issues at the solid electrode-electrolyte interface [75-81]. From electrochemistry aspect, solid electrolytes, even though having a wide electrochemical stability window, can still decompose during battery operation, forming SEI and cathode electrolyte interphase (CEI) layers at the solid electrode-electrolyte interface. If the SEI and CEI are electronically conductive, then the interphases will continue to grow and lead to larger interface impedance and capacity fading of SSBs [77-79]. From mechanical aspect, the stress generated in electrodes during Li insertion/extraction now interacts with solid electrolytes, and the solid-solid contact at the interface can cause multiple problems: First, during SSB cycling, the shearing stress at the interface induced by electrode expansion/contraction can promote Li dendrite

growth in solid electrolyte layer and eventually shorts the battery. Second, electrochemical kinetics is coupled with mechanical stress at the interface, and in the case of SSB, both electrode and solid electrolyte contribute to the ECM effect, leading to a more complex ECM coupling than the case in traditional liquid-based battery systems. Lastly, delamination of electrode from solid electrolyte can occur when the interfacial shearing stress exceeds the bonding strength between electrolyte and solid electrolyte. Therefore, understanding of ECM interaction at the solid electrode-electrolyte interface is a key challenge for further advancement of SSBs.

Interface study in SSB is not as straightforward as in liquid-based battery, because the capping layer in SSB is usually a metal current collector, which blocks optical and electron beam access to the interface. In a typical interface study in SSB, focused ion beam (FIB) is applied to cut a thin slice along the cross section of SSB [82,83]. The obtained thin slice is then mounted on a special TEM holder with electrically connection to current collectors of SSB and in the following, it is transferred to TEM for additional imaging and spectroscopy studies. This technique involves tedious sample preparation and large cell impedance. Additionally, the thin slice battery is air sensitive and requires high vacuum condition during transfer and characterization. Therefore, it will be ideal if the cross-section of SSB can be transferred onto a 2D plane, where all battery layers can be viewed from the topside.

In this chapter, we present a SSB platform device with lateral configuration where all battery layers are partly distributed in the same plane. We patterned this device through thin film depositions and photolithography, to precisely control the gap size of solid electrolyte. With 4um gap of solid electrolyte, a symmetric Li_xSi-Si solid state cell showed cell impedance of ~100MΩ and active electrochemistry. In addition, the cell was protected by a Al_2O_3 capping layer, which enabled in-air operation with comparable electrochemistry activity as in the glovebox. Furthermore, through Raman measurement and FEA modeling, we validate this lateral SSB as a platform device for stress characterization, and it can serve as more versatile platform for other interface studies.

5.2 Experimental

5.2.1 Device fabrication

The fabrication of the lateral SSB device consists of six steps: First, a thin Al_2O_3 layer (~60nm) was deposited through ALD process. Second, a W thin film (~100nm) was deposited through sputtering and patterned by photolithography and RIE etching. The patterned W layer serves as current collector for both working and counter electrodes. Third, an amorphous Si thin film (~300nm), serving as working electrode, was deposited through PECVD process and patterned through photolithography and RIE etching. Fourth, another a-Si, serving as counter electrode

(~300nm), was deposited by PECVD process. The counter electrode layer will then be patterned through similar photolithography and etching process as the working electrode. Next, the patterned counter electrode was pre-lithiated in a beaker cell. Lastly, the device with prelithaited counter electrode was transferred to sputtering tool for LiPON and Al_2O_3 deposition. Here, Al_2O_3 serves as a protective layer to avoid chemical degradation of solid electrolyte when exposed to air.

5.2.2 Electrochemistry

CV and EIS were performed on solid state cells to assess their electrochemical activity and cell impedance. CV was conducted at various potential ranges with sweep rate of 0.5mV/s and EIS was conducted at frequency range from 800Mhz to 10mHz.

5.2.3 μ-Raman spectroscopy

During Raman measurement, a 100X dry objective lens with NA0.8 was used (Olympus, LMPLANFL N). 532nm laser (GaAs) with D2 intensity filter were used, and the incident laser power was controlled to 1mW. 200um hole and 100um slit were used to enhance confocality and for each acquisition, 2s exposure and 0.5um step space were used.

5.3 Results and discussion

5.3.1 SSB platform design

The proposed geometry for the lateral SSB is shown in figure 5.1(a). As a goal to transfer the cross-section of SSB onto a 2D plane, in this device, every battery component is partly distributed in the same plane. In this design, because the solid electrolyte LiPON has much lower electronic conductivity[84] ($\sigma_e = 8 \times 10^{-14}\,\mathrm{S/cm}$) than a-Si electrodes ($\sigma_e = 10^{-9}\,\mathrm{S/cm}$), the electric potential primarily drop between the edges of electrodes and form a lateral electric field. Therefore, the Li ions will pass preferentially through the edge of electrodes. This device, in principle, give access to interface and chemical compositional study in the SSB, as all interfaces and battery components are directly exposed to the top surface. In addition, the stress generated in the electrodes will interact with the single-c Si substrate, which can be used as stress reporter for in-situ stress characterization. Lastly, a larger area (~0.5cm^2) for counter electrode than working electrode (~0.001cm^2) was designed, so the counter electrode can serve as a semi-infitinite Li source, and thus, serve as reference electrode.

The fabrication process for this SSB platform device is elaborated in experimental section and shown in figure 5.1(b). In this device, ALD Al_2O_3 layer served as an electronic insulator between Si wafer substrate and the SSB to avoid

electrical shortage. Al_2O_3 was also compatible with the overall fabrication process, as it served as a stop layer for fluorine-based plasma etching in the following steps. In addition, another Al_2O_3 layer on top of the SSB device was used for encapsulation and protecting the device from air exposure.

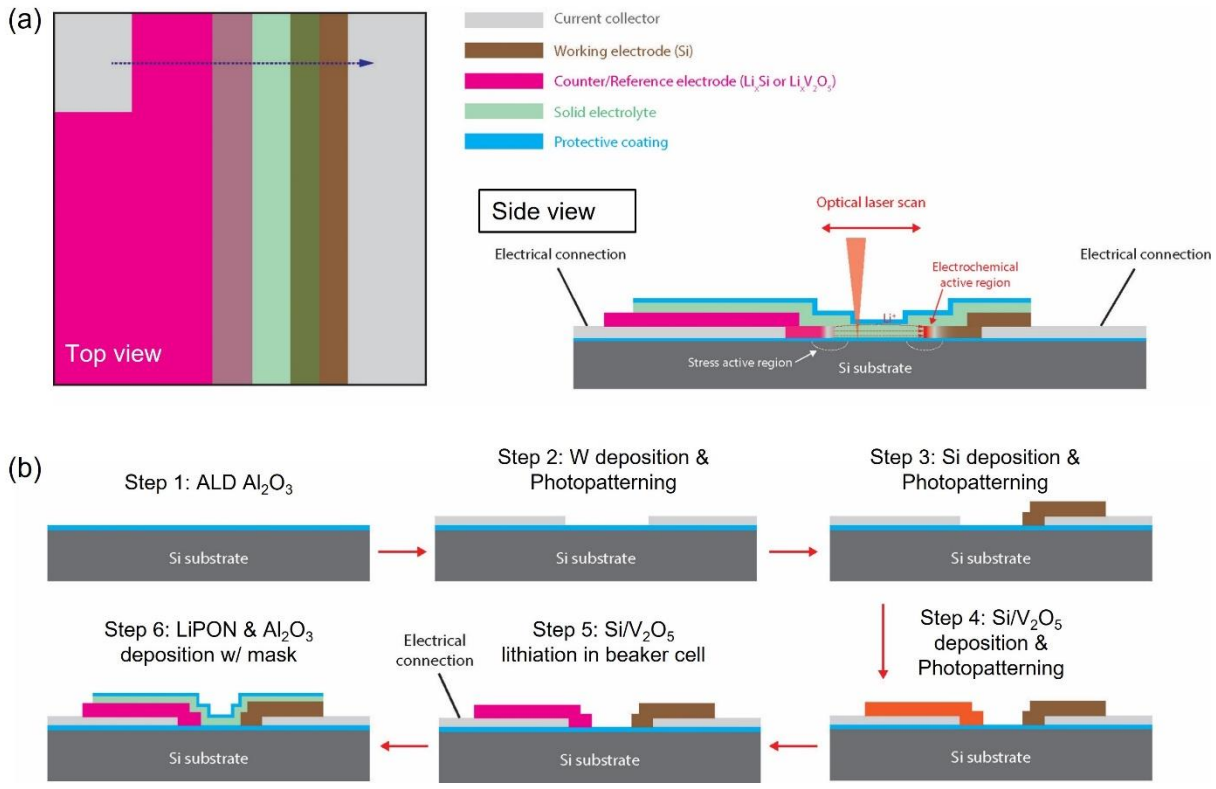

Figure 5. 1: (a) Schematic of lateral SSB design and (b) the associated fabrication process.

5.3.2 Sample characterization

In this work, we demonstrate a Si-Si symmetric solid state cell as a proof of concept for the lateral SSB design. In each batch, 28 devices with different dimensional parameters such as gap size for electrolyte and electrodes geometries,

were fabricated on a single 3inch Si wafer, and a picture of devices after fabrication is shown in figure 5.2(a). One of the patterned Si-Si device (corresponding to the device after step 4 in figure 5.1(b)) is shown in figure 5.2(b). SEM image, as shown in figure 5.2(b), has shown that a well-defined geometry patterned through the proposed fabrication process with a gap size of 4um between electrodes was obtained. In the prelithiation step, the electrochemistry of PECVD a-Si was characterized through CV in a potential range between 60mV and 1.4V, as shown in figure 5.2(c). During lithiation, clear reduction peak was not observed. Instead, a sharp increase of reduction current occurred at potential of ~0.4V. However, in the delithaition process, a clear oxidation peak at ~0.5V was observed. This is probably due to the nature of amorphous phase of the PECVD Si, as similar CV curve has also been reported in prior literature [85-86]. In addition, at sweep rate of 0.5mV/s, the magnitude of current density (~500-1000uA/cm^2) of this a-Si was larger than crystalline Si by an order of magnitude (~50uA/cm^2). This is probably due to weaker Si-Si bonding in the a-Si, which lowered the energy barrier for Li diffusion and promotes the electrochemical kinetics of Li ion reduction at the electrode-electrolyte interface. Similar cyclic voltammetry of a-Si thin film electrode in liquid half-cell was also reported in another study [87].

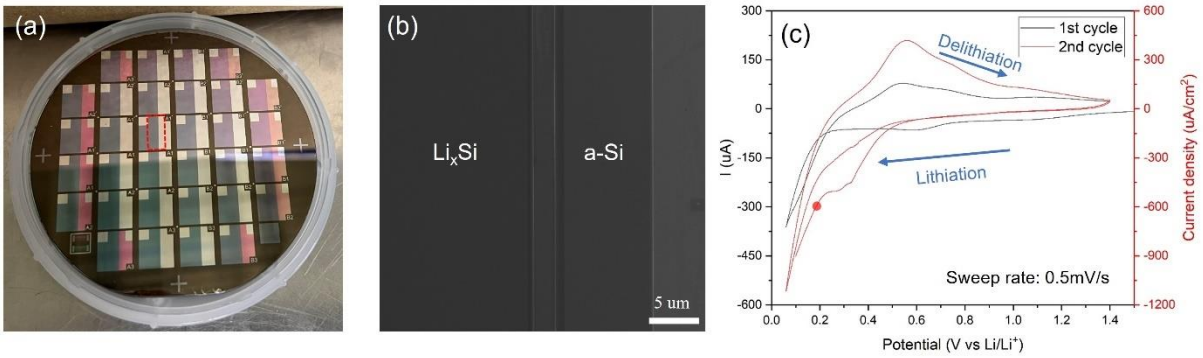

Figure 5. 2: (a) Image of fabricated device with patterned working and counter electrodes (Si-Si cells) (b) SEM image of a single device, corresponding to the red dashed rectangle in (a). (c) Cyclic voltammetry of PECVD a-Si. The red dot indicates the potential that is held during prelithaition step (0.2V).

Image of a fully fabricated solid-state cell, with Li_xSi counter/reference electrode, is shown in figure 5.3(a). Area of LiPON and Al_2O_3 patterned by shadow masking is indicated in red dashed lines. SEM image of the cross-section in the solid-state cell, as shown in figure 5.3(b), shows separated electrodes with sharp edges and conformal coating of LiPON. The red dashed rectangle area is shown in figure 5.3(c), which indicates a profile of the solid state cell with 380nm LiPON, 300nm Si, 60nm of W, and 60nm of Al_2O_3. The exact thickness of Al_2O_3 cap layer on the top surface was not measured due to low contract in the image.

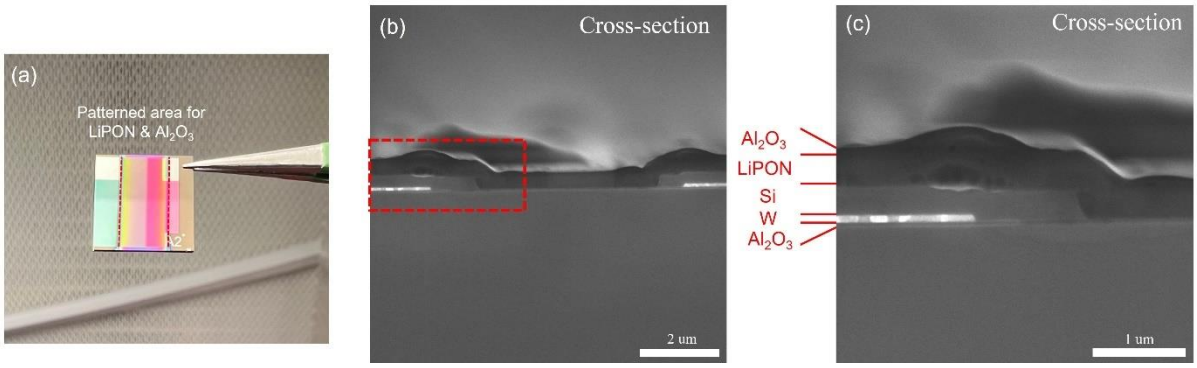

Figure 5. 3: (a) Image of a Li_xSi-Si solid state cell. (b) SEM cross-sectional image of the cell. (c) High magnication SEM image corresponding to the red dashed rectangle area in (b).

5.3.3 Electrochemistry of Si-Si symmetric cell and in-air operation

Electrochemistry test of the Li_xSi-Si symmetric cell was first conducted in a glovebox, using cyclic voltammetry at sweep rate of 0.5mV/s. Different potential ranges were used to assess the overpotential caused by the 4um size gap of LiPON. In figure 5.4 (a), CV of the solid-state cell showed Li ion storage, indicating a electrochemically working cell. In addition, OCV of the cell showed a stable value at -0.4V after first electrochemical cycling, indicating that the potential of prelithiated Li_xSi counter electrode was stable. From the CV result, clear redox peaks were not observed even at the largest potential range between -2V to 1.6V, except a broad peak in the potential range between -2V to -0.5V. This was an oxidation peak from Li_xSi counter electrode, which was also observed in the CV curve of a-Si in liquid half-cell. The magnitude of total current in this cell during cycling was in the order of 10nA, attributed to the small area on the edge of electrodes and large cell impedance (~70MΩ), as shown in figure 5.4(b). The current density, however, was

in the order of ~100uA/cm^2 assuming that the edge of the electrodes is the only active area. This is consistent with the CV result obtained from liquid half-cell. The exact surface area of electrodes that is electrochemically active in this cell needs further ex-situ characterization from other complimentary techniques such as TEM and EELs.

Next, electrochemistry of the solid state-cell was tested in the air. CV result from in-air testing is shown in figure 5.5(a). Similar CV curve was observed as compared to the case in glovebox, while the magnitude of current was slightly smaller. This is caused by increased cell impedance after moving from glovebox to the air, as indicated by the EIS result shown in figure 5.5(b). The impedance increased from ~70MΩ to ~90MΩ, and after 6hours testing in the air, the impedance further shifted to ~100 MΩ. The EIS result indicates that the cell is relatively stable in the air during the 6hour timeframe of this test.

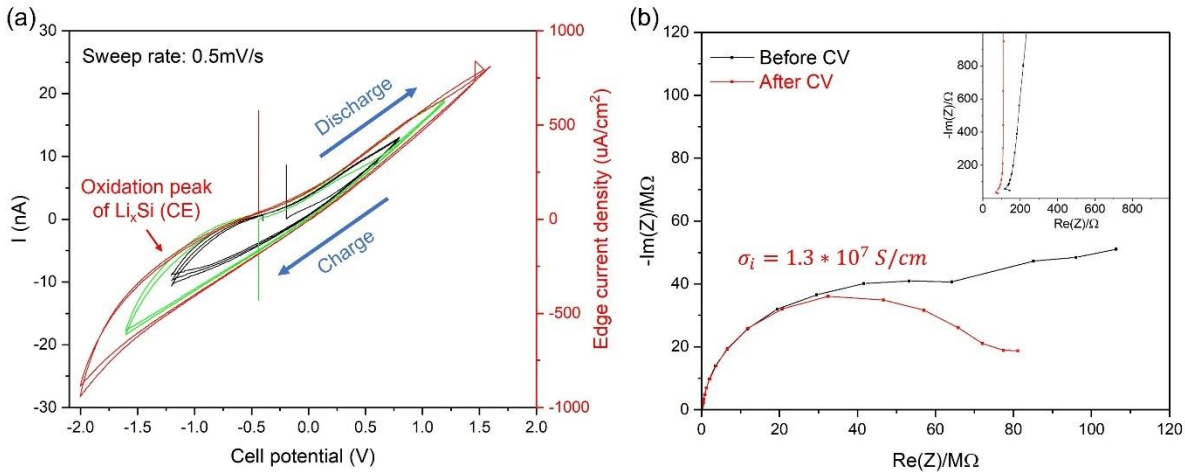

Figure 5. 4: (a) CV curve of the Li$_x$Si-Si solid state cell. (b)EIS of the cell before and after CV test, in the frequency range between 800kHz and 10mHz.

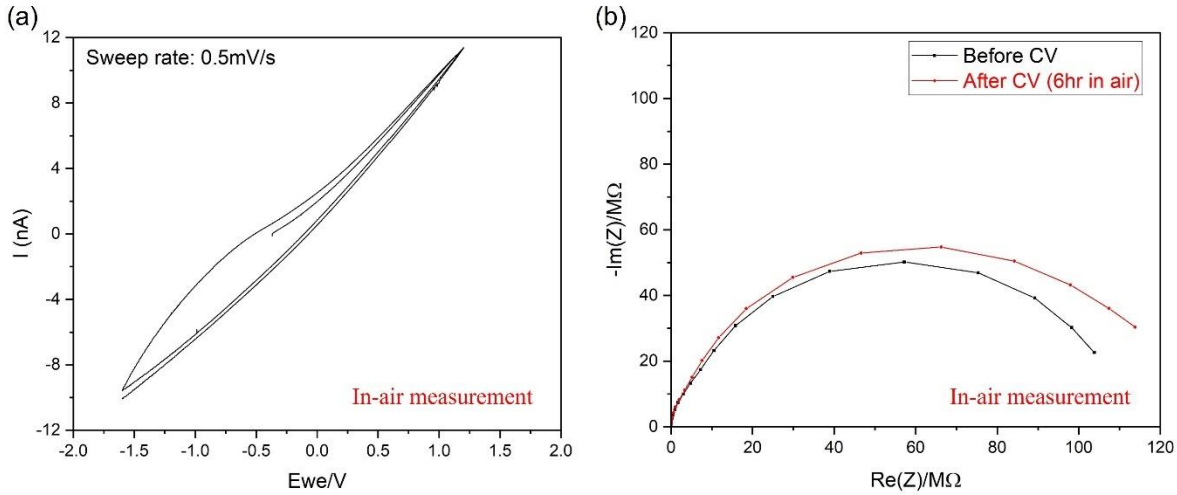

Figure 5. 5: In-air testing of Li$_x$Si-Si symmetric cell and the corresponding (a) CV and, (b) EIS results.

5.3.4 Raman stress measurement and platform validation

To demonstrate the SSB device as a platform for stress characterization, Raman stress measurement was carried out by performing line scan across the cell surface, as shown in figure 5.6(a). Two ex-situ measurement were performed on as-fabricated sample (Si-Si pads without prelithiation) and SSB after cycling, and the

line scan results are shown in figure 5.6(b). First, for the as-fabricated sample, it showed tensile stress at the edge of both electrodes. This was residual stress caused by the lattice mismatch between PECVD a-Si and Si substrate. Second, the cycled solid-state cell showed a stronger tensile stress in the prelithiated Si region, while on the opposite side, the a-Si working electrode showed smaller shift to the tensile stress. The results fitted the expectation since Li insertion introduced tensile stress in Si electrodes. However, it should be noted that the magnitude of tensile stress is in the order of ~50MPa, which is the stress value reflected on Si substrate. To quantitatively assess the stress that's actually generated by active Si electrode, an additional step needs to be taken to calculate the mechanical interaction between Si electrode and Si substrate.

To answer the question and further validate the strategy of using Si substrate as stress reporter in the SSB platform device, we established a FEM model using solid mechanics and heat transfer physics. In this model, we used heat transfer to mimic the Li ion insertion/extraction process in Si, and the volumetric stress induced by heating or cooling interacted with Si substrate through mechanical processes. The modeled geometry and boundary conditions are shown in figure 5.7 (a) and (b). In this model, we built two Si thin rectangles with width of 10um and thickness of 300nm on the top surface, to represent the Si counter and working electrodes. 60nm of Al_2O_3 layer was placed between electrodes and Si substrate. Additionally, since

penetration depth of 532nm laser in Si in ~0.7um [88], a rectangular area with width of 6um and thickness of 0.5um sitting under Al_2O_3 layer was defined to represent the Raman probing volume during Raman measurement. The stress generated in this rectangular area was averaged along the y-axis to obtain an average stress value, which was compared with the stress value obtained from Raman measurement.

The averaged stress in the top electrodes is shown in figure 5.7(c), where the tensile stress on the counter electrode was released as Li was continuously removed, while on the opposite side, the tensile stress got stronger as Li inserted. On the other hand, the stress in Raman probing region showed a similar change of stress, with less tensile stress at the edge of counter electrode and higher tensile stress at the edge of working electrode. In addition, the stress generated at the edge of electrode layer was larger than the stress in Raman probing region by a factor of ~6. This correlation indicates that the measured stress from Raman line scan implies a stress from the top electrode with order of magnitude ~300MPa. Considering that the lithiation induced stress in Si is typical in the order of hundreds of MPa, this correlation shows promise of our strategy of using Si substrate as a stress reporter.

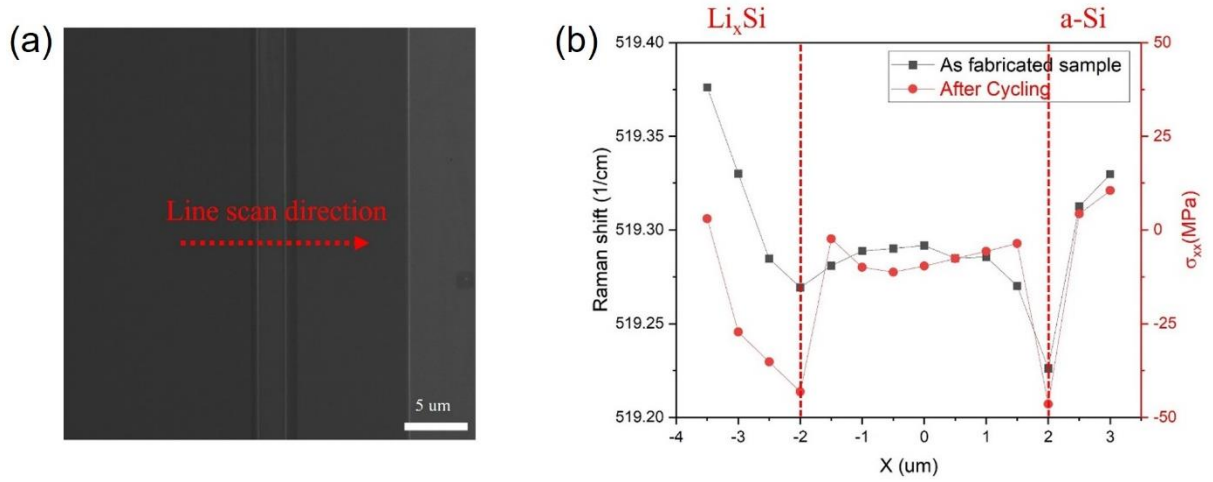

Figure 5. 6: (a) SEM image of Si-Si symmetric device and line scan direction during Raman measurement. (b) Stress distribution across the Si-Si device after fabrication and Li_xSi-Si symmetric cell after cycling.

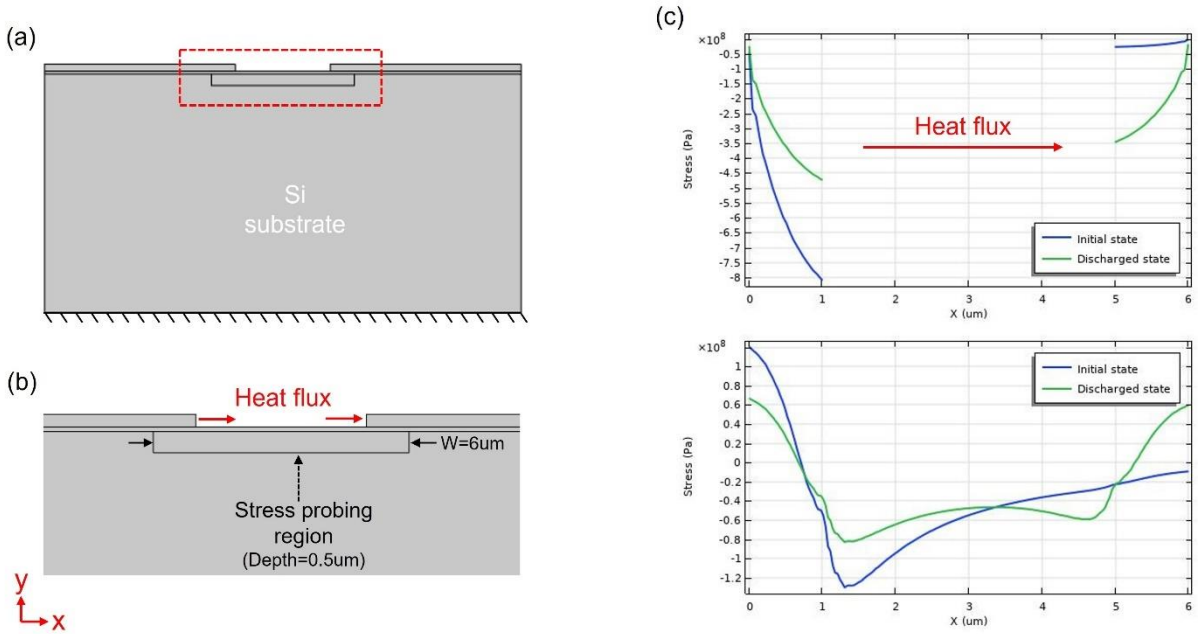

Figure 5. 7: (a) Geometry of Heat-mechanics model setup and (b) the boundary condition applied to the model. (c) Stress distribution in the top electrodes layer (result was averaged along y axis from the bottom of electrodes layer to the top surface) (d) Stress distribution in the stress probing region (also averaged along y axis from the bottom side to the top side of probing region)

5.4 Conclusion

In this chapter, we demonstrated an intriguing SSB design with lateral configuration. As a proof of concept, we built the cell with Si as both working and counter electrodes, while the fabrication strategy can be applied to a wide spectrum of other electrode materials to investigate different LIB systems. With Al_2O_3 protective coating, the symmetric cell showed active electrochemistry and stability in the air for at least 6 hours. Raman stress measurement also showed active stress response from cycled cell, and through FEM modeling, we demonstrated that the magnitude of average stress generated in the electrode dropped by a factor of 6 when it was reflected in the Si substrate during Raman measurement. Although further study of this lateral SSB is still ongoing, we have demonstrated a novel route for creating SSB that can be used for in-situ study with relatively easy access to the interfaces. We hope this device could bring more advanced interface studies of SSBs.

Chapter 6: Conclusions and outlook

6.1 Summary

ECM coupling is a ubiquitous effect in alloying type electrodes, as volume change associated with Li insertion/extraction introduces stress, which in turn affects the electrochemical kinetics and mechanical failure of the electrodes. Understanding the ECM coupling effect in alloying type electrodes such as Si is thus of critical importance for its application in high energy density LIB systems. However, detailed experimental study of ECM coupling is challenging, since slow Li diffusion kinetics in alloying type electrodes typical introduce a large stress gradient, and resolving the stress distribution requires characterization techniques that have scanning capabilities. Raman spectroscopy is one of the techniques that can spatially resolve stress distribution and has been widely used in the past for stress characterization in Si based semiconductor devices. However, Raman spectroscopy for stress characterization in the electrochemical studies of Si electrodes has not been widely adopted. This is due to the instability of liquid electrolyte at the working potential of Si electrode. The organic decomposition product of liquid electrolyte, i.e. SEI layer, forms on the surface of Si electrode during Li insertion and impedes the laser access to the surface of Si. Overcoming this challenge requires advanced strategies. This

dissertation presents a three-phase study that used different strategies to overcome this issue and provide a route for successful stress measurement in Si electrode.

In the first phase, an ex-situ Raman stress measurement was performed on bulk single-c Si electrodes, to validate μ-Raman as a promising stress measurement technique for Si electrodes. In this study, SEI layer was removed by organic solvent and Raman measurement was performed on the cross-section of Si electrodes. A surprising c-Li_xSi layer was found in between a-Li_xSi and c-Si layers. The origin of this intermediate layer was proposed to be a consequence of mechanical constraint imposed on the Si electrode, which enhanced Li diffusion in c-Li. In addition, the stress distribution in lithiated single-c Si electrode was measured and stress relaxation at lithiation front, attributed to plastic flow at the interface, was observed. The flow stress measured by ex-situ Raman experiment was compared with in-situ MOS results obtained from prior literature and showed a consistent trend. Lastly, the stress distribution in single-c Si electrodes after initial delithiation was measured and cracking mechanism at different cycling conditions was explored and explained.

In the second phase, an in-situ Raman stress measurement was conducted on patterned poly-c Si thin film electrodes, to explore the correlation between complex geometries and stress distribution in Si electrode. In this study, an in-situ experiment setup coupled with novel electrochemical cell was established and showed a scanning resolution of ~0.5um. To overcome the challenge of SEI layer formation,

Si thin film was used so that the penetration depth was limited to the thickness of thin film, rounding to smaller average effect as compared to bulk single-c Si. In addition, lithiation potential of Si thin film electrode was selected so that there's lithiation occurs in Si but thick SEI layer doesn't form. Undesired Tungsten oxide formation was observed, and by electrochemical treatment, the tungsten oxide was lithiated thoroughly and conditioned for additional poly-c Si layer testing. At different potential, stress distribution in poly-c Si thin film electrodes during charge and discharge was measured, and the kinetic response of poly-c Si electrodes with different size was analyzed and compared with FEM modeling. A comprehensive understanding was obtained and the critical size effect in patterned poly-c Si electrode was explained.

In the last phase, to investigate the stress of Si electrode in solid state battery system, a SSB platform device was proposed. In this study, SEI issue was completely avoided as solid electrolyte, specifically, LiPON, has a much wider electrochemical stability window than typical liquid electrolytes. The electrochemistry activity of this device was proven, and it showed stability in the air for at least six hours, which is typically sufficient for most of battery characterizations. By using FEM modeling, the correlation between Raman measured stress and the stress in Si electrode was established and the magnitude of experimental results showed consistency with

typical lithiation induced stress. Besides stress characterization, the SSB platform device can serve as a versatile testbed for other interface studies for SSB.

In summary, this dissertation presents an advanced methodology that combines μ-Raman spectroscopy and novel electrochemical test devices for stress characterization in Si electrodes. With help of FEM modeling, an intriguing understanding of ECM effect in Si electrodes was obtained and showed good consistency with prior literature.

6.2 Future directions

6.2.1 Origin of c-Li_xSi layer

In chapter three, a c-Li_xSi layer with thickness of ~800nm was found in lithiated single-c Si electrode. The presence of this layer with such thickness has never been reported, and it has two indications of ECM effect in Si electrode: First, diffusion coefficient is affected by not only stress, but also stress gradient, as discussed in chapter three. Second, the stable thickness of c-Li_xSi layer indicates that there's a dynamic balance between electrochemical reaction at the interface and lithium diffusion in Si lattice. Further experiments are needed to investigate the thickness change of the c-Li_xSi by controlling the mechanical constraint of single-c Si electrode. TEM characterization is also desired, to investigate the crystalline structure and Li concentration variation in the c-Li_xSi layer. Lastly, FEM modeling

will be crucial to help fully explain the origin of this layer and the associated ECM coupling effect.

6.2.2 Raman shift of Li_xSi

During Raman stress characterization, the presence of c-Li_xSi layer give rise to an additional question: In c-Li_xSi layer, the Raman shift was induced by internal stress, i.e. Li insertion induced stress. However, the correlation between Raman shift and state of charge in Si electrode is not established. To establish the correlation, experimental methods are pretty limited, as c-Li_xSi is not thermal dynamically stable (at RT) when $x<1$. Thermally stable phases include LiSi, Li_7Si_3, $Li_{13}Si_4$, $Li_{12}Si_7$, and $Li_{22}Si_5$. But except LiSi, all other phases have different crystalline structures from diamond structure [89,90] and thus are not helpful for establishing the correlation. As an alternative, first-principle calculation has potential to provide insight in this. The vibrational frequency of phonon modes at different lithiation level of Si can be calculated, and the calculation methodology can be transferred to other crystalline electrodes and help standardize Raman spectroscopy as stress characterization techniques in electrochemical systems.

6.2.3 Current collector for Si based model devices

In chapter four and five, W was chosen as current collector for Si electrode model devices based on a few factors: 1. Electrochemical inertness. 2. Thermal stability. 3.

Formation temperature of silicide. 4. Process compatibility with deposition and etching processes of other battery thin film materials. W metal is a promising current collector material as it doesn't electrochemically alloy with Li. In addition, W has high thermal stability (melting point @ 3422^{o}C) and can be removed by plasma etching using fluorine-based gas chemistry. The fluorine-based plasma etching is an important etching technique for Si based device since it has high selectivity between Si and other oxide materials. Therefore, W current collector can be patterned with high spatial resolution and enable well defined geometries of Si based devices. Lastly, formation temperature of WSi_2 is at above 650^{o}C, which enables integration of W current collector with poly-c Si electrodes. However, at elevated temperature (@ ~300^{o}C), tungsten oxide can form and cause parasitic electrochemical reaction in Si electrode devices, as has been observed in chapter four. Finding another current collector material with better chemical inertness, such as Au and Pt, or careful processing W current collector to avoid oxide formation will be critical for better controlling the electrochemistry in Si electrode model devices.

6.2.4 ECM effect in 3D-SSB

In the pursuit of high energy and power density, SSBs are often designed into 3D architectures. However, the complex geometries inevitably involve sharp corners, which can diverge or concentrate the electric field, leading to a nonuniform

distribution of Li concentration and stress along the solid electrode-electrolyte interface. It is thus intriguing to measure the stress distribution at the interface and understand whether sharp corners facilitate or degrade the performance of 3D-SSBs. This study can be performed using the SSB platform device proposed in chapter five, as the cross-section in 3D-SSB can be transformed onto a 2D plane in this platform device by patterning the electrodes into conformal geometries. In this case, stress distribution in SSB can be directly measured and the understanding obtained from this study can pave a way for future 3D-SSB design.

Bibliography

1. Folkson, R. *Alternative Fuels and Advanced Vehicle Technologies for Improved Environmental Performance : Towards Zero Carbon Transportation*; Woodhead Publishing: Oxford, 2016.
2. Bashir, T., Ismail, S. A., Song, Y., Irfan, R. M., Yang, S., Zhou, S., ... & Gao, L. (2021). A review of the energy storage aspects of chemical elements for lithium-ion based batteries. *Energy Materials*, *1*(2), 100019.
3. U.S. Energy Information Administration, 2021, 3.
4. Ni, J., Dai, A., Yuan, Y., Li, L., & Lu, J. (2020). Three-dimensional microbatteries beyond lithium ion. *Matter*, *2*(6), 1366-1376.
5. Pearse, A., Schmitt, T., Sahadeo, E., Stewart, D. M., Kozen, A., Gerasopoulos, K., ... & Gregorczyk, K. E. (2018). Three-dimensional solid-state lithium-ion batteries fabricated by conformal vapor-phase chemistry. *ACS nano*, *12*(5), 4286-4294.
6. Mukhopadhyay, A., & Sheldon, B. W. (2014). Deformation and stress in electrode materials for Li-ion batteries. *Progress in Materials Science*, *63*, 58-116.
7. Zhu, Y., He, X., & Mo, Y. (2015). Origin of outstanding stability in the lithium solid electrolyte materials: insights from thermodynamic analyses based on first-principles calculations. *ACS applied materials & interfaces*, *7*(42), 23685-23693.
8. Plashnitsa, L. S., Kobayashi, E., Noguchi, Y., Okada, S., & Yamaki, J. I. (2010). Performance of NASICON symmetric cell with ionic liquid electrolyte. *Journal of the Electrochemical Society*, *157*(4), A536.
9. Han, F., Zhu, Y., He, X., Mo, Y., & Wang, C. (2016). Electrochemical stability of Li10GeP2S12 and Li7La3Zr2O12 solid electrolytes. *Advanced Energy Materials*, *6*(8), 1501590.
10. Choi, N. S., Yew, K. H., Lee, K. Y., Sung, M., Kim, H., & Kim, S. S. (2006). Effect of fluoroethylene carbonate additive on interfacial properties of silicon thin-film electrode. *Journal of Power Sources*, *161*(2), 1254-1259.
11. Mukhopadhyay, A., & Sheldon, B. W. (2014). Deformation and stress in electrode materials for Li-ion batteries. *Progress in Materials Science*, *63*, 58-116.
12. Rhodes, K., Dudney, N., Lara-Curzio, E., & Daniel, C. (2010). Understanding the degradation of silicon electrodes for lithium-ion batteries using acoustic emission. *Journal of the Electrochemical Society*, *157*(12), A1354.
13. Xu, R., & Zhao, K. (2016). Electrochemomechanics of electrodes in Li-ion batteries: A review. *Journal of Electrochemical Energy Conversion and Storage*, *13*(3).
14. Weber, W. (1977). Adiabatic bond charge model for the phonons in diamond, Si, Ge, and α− Sn. *Physical Review B*, *15*(10), 4789.
15. Ganesan, S., Maradudin, A. A., & Oitmaa, J. (1970). A lattice theory of morphic effects in crystals of the diamond structure. *Annals of Physics*, *56*(2), 556-594.
16. Anastassakis, E., Pinczuk, A., Burstein, E., Pollak, F. H., & Cardona, M. (1993). Effect of static uniaxial stress on the Raman spectrum of silicon. *Solid State Communications*, *88*(11-12), 1053-1058.
17. De Wolf, I. (1996). Micro-Raman spectroscopy to study local mechanical stress in silicon integrated circuits. *Semiconductor science and technology*, *11*(2), 139.
18. Krause, A., Tkacheva, O., Omar, A., Langklotz, U., Giebeler, L., Dörfler, S., ... & Weber, W. M. (2019). In situ Raman spectroscopy on silicon nanowire anodes integrated in lithium ion batteries. *Journal of The Electrochemical Society*, *166*(3), A5378.
19. Cao, C., Steinrück, H. G., Shyam, B., Stone, K. H., & Toney, M. F. (2016). In situ study of silicon electrode lithiation with X-ray reflectivity. *Nano letters*, *16*(12), 7394-7401.
20. Pharr, M., Zhao, K., Wang, X., Suo, Z., & Vlassak, J. J. (2012). Kinetics of initial lithiation of crystalline silicon electrodes of lithium-ion batteries. *Nano letters*, *12*(9), 5039-5047.
21. Zhang, S. (2017). Chemomechanical modeling of lithiation-induced failure in high-volume-change electrode materials for lithium ion batteries. *npj Computational Materials*, *3*(1), 1-11.
22. Yang, F. (2005). Interaction between diffusion and chemical stresses. *Materials Science and Engineering: A*, *409*(1-2), 153-159.
23. Sethuraman, V. A., Srinivasan, V., Bower, A. F., & Guduru, P. R. (2010). In situ measurements of stress-potential coupling in lithiated silicon. *Journal of the Electrochemical Society*, *157*(11), A1253.
24. Loudon, R. (1964). The Raman effect in crystals. Advances in Physics, 13(52), 423-482.

25. Beechem, T., Graham, S., Kearney, S. P., Phinney, L. M., & Serrano, J. R. (2007). Invited Article: Simultaneous mapping of temperature and stress in microdevices using micro-Raman spectroscopy. *Review of Scientific Instruments*, *78*(6), 061301.
26. Anastassakis, E., Cantarero, A., & Cardona, M. (1990). Piezo-Raman measurements and anharmonic parameters in silicon and diamond. *Physical Review B*, *41*(11), 7529.
27. Brantley, W. A. (1973). Calculated elastic constants for stress problems associated with semiconductor devices. *Journal of Applied Physics*, *44*(1), 534-535.
28. Shi, F.; Song, Z.; Ross, P. N.; Somorjai, G. A.; Ritchie, R. O.; Komvopoulos, K. Failure Mechanisms of Single-Crystal Silicon Electrodes in Lithium-Ion Batteries. *Nature Communications* **2016**, *7* (1). DOI:10.1038/ncomms11886.
29. Wu, H.; Cui, Y. Designing Nanostructured Si Anodes for High Energy Lithium Ion Batteries. *Nano Today* **2012**, *7* (5), 414–429. DOI:10.1016/j.nantod.2012.08.004.
30. Liu, N.; Wu, H.; McDowell, M. T.; Yao, Y.; Wang, C.; Cui, Y. A Yolk-Shell Design for Stabilized and Scalable Li-Ion Battery Alloy Anodes. *Nano Letters* **2012**, *12* (6), 3315–3321. DOI:10.1021/nl3014814.
31. Wu, H.; Chan, G.; Choi, J. W.; Ryu, I.; Yao, Y.; McDowell, M. T.; Lee, S. W.; Jackson, A.; Yang, Y.; Hu, L.; Cui, Y. Stable Cycling of Double-Walled Silicon Nanotube Battery Anodes through Solid–Electrolyte Interphase Control. *Nature Nanotechnology* **2012**, *7* (5), 310–315. DOI:10.1038/nnano.2012.35.
32. Liu, N.; Lu, Z.; Zhao, J.; McDowell, M. T.; Lee, H.-W.; Zhao, W.; Cui, Y. A Pomegranate-Inspired Nanoscale Design for Large-Volume-Change Lithium Battery Anodes. *Nature Nanotechnology* **2014**, *9* (3), 187–192. https://doi.org/10.1038/nnano.2014.6.
33. Chan, C. K.; Peng, H.; Liu, G.; McIlwrath, K.; Zhang, X. F.; Huggins, R. A.; Cui, Y. High-Performance Lithium Battery Anodes Using Silicon Nanowires. *Nature Nanotechnology* **2007**, *3* (1), 31–35. https://doi.org/10.1038/nnano.2007.411.
34. Yang, L. Y.; Li, H. Z.; Liu, J.; Sun, Z. Q.; Tang, S. S.; Lei, M. Dual Yolk-Shell Structure of Carbon and Silica-Coated Silicon for High-Performance Lithium-Ion Batteries. *Scientific Reports* **2015**, *5* (1).
35. Cui, L. F., Ruffo, R., Chan, C. K., Peng, H., & Cui, Y. (2009). Crystalline-amorphous core− shell silicon nanowires for high capacity and high current battery electrodes. *Nano letters*, *9*(1), 491-495.
36. Chon, M. J.; Sethuraman, V. A.; McCormick, A.; Srinivasan, V.; Guduru, P. R. Real-Time Measurement of Stress and Damage Evolution during Initial Lithiation of Crystalline Silicon. *Physical Review Letters* **2011**, *107* (4). https://doi.org/10.1103/physrevlett.107.045503.
37. Sethuraman, V. A.; Chon, M. J.; Shimshak, M.; Srinivasan, V.; Guduru, P. R. In Situ Measurements of Stress Evolution in Silicon Thin Films during Electrochemical Lithiation and Delithiation. *Journal of Power Sources* **2010**, *195* (15), 5062–5066. https://doi.org/10.1016/j.jpowsour.2010.02.013.
38. Sethuraman, V. A.; Van Winkle, N.; Abraham, D. P.; Bower, A. F.; Guduru, P. R. Real-Time Stress Measurements in Lithium-Ion Battery Negative-Electrodes. *Journal of Power Sources* **2012**, *206*, 334–342. https://doi.org/10.1016/j.jpowsour.2012.01.036.
39. Yang, H., Liang, W., Guo, X., Wang, C. M., & Zhang, S. (2015). Strong kinetics-stress coupling in lithiation of Si and Ge anodes. *Extreme Mechanics Letters*, *2*, 1-6.
40. Xiao, X.; Liu, P.; Verbrugge, M. W.; Haftbaradaran, H.; Gao, H. Improved Cycling Stability of Silicon Thin Film Electrodes through Patterning for High Energy Density Lithium Batteries. *Journal of Power Sources* **2011**, *196* (3), 1409–1416. https://doi.org/10.1016/j.jpowsour.2010.08.058.
41. Zhao, K.; Pharr, M.; Wan, Q.; Wang, W. L.; Kaxiras, E.; Vlassak, J. J.; Suo, Z. Concurrent Reaction and Plasticity during Initial Lithiation of Crystalline Silicon in Lithium-Ion Batteries. *Journal of The Electrochemical Society* **2012**, *159* (3), A238–A243. DOI:10.1149/2.020203jes.
42. Zeng, Z., Liu, N., Zeng, Q., Lee, S. W., Mao, W. L., & Cui, Y. (2016). In situ measurement of lithiation-induced stress in silicon nanoparticles using micro-Raman spectroscopy. *Nano Energy*, *22*, 105-110.
43. Tardif, S., Pavlenko, E., Quazuguel, L., Boniface, M., Maréchal, M., Micha, J. S., ... & Lyonnard, S. (2017). Operando Raman spectroscopy and synchrotron X-ray diffraction of lithiation/delithiation in silicon nanoparticle anodes. *ACS nano*, *11*(11), 11306-11316.
44. Jana, M.; Singh, R. N. A Study of Evolution of Residual Stress in Single Crystal Silicon Electrode Using Raman Spectroscopy. *Applied Physics Letters* **2017**, *111* (6), 063901. https://doi.org/10.1063/1.4997768.
45. Krause, A., Tkacheva, O., Omar, A., Langklotz, U., Giebeler, L., Dörfler, S., ... & Weber, W. M. (2019). In situ Raman spectroscopy on silicon nanowire anodes integrated in lithium ion batteries. *Journal of The Electrochemical Society*, *166*(3), A5378.

46. McDowell, M. T., Lee, S. W., Nix, W. D., & Cui, Y. (2013). 25th anniversary article: understanding the lithiation of silicon and other alloying anodes for lithium-ion batteries. *Advanced Materials*, *25*(36), 4966-4985.
47. Limthongkul, P., Jang, Y. I., Dudney, N. J., & Chiang, Y. M. (2003). Electrochemically-driven solid-state amorphization in lithium-silicon alloys and implications for lithium storage. *Acta Materialia*, *51*(4), 1103-1113.
48. Liu, X. H., Wang, J. W., Huang, S., Fan, F., Huang, X., Liu, Y., ... & Huang, J. Y. (2012). In situ atomic-scale imaging of electrochemical lithiation in silicon. *Nature nanotechnology*, *7*(11), 749-756.
49. Cao, C., Steinrück, H. G., Shyam, B., Stone, K. H., & Toney, M. F. (2016). In situ study of silicon electrode lithiation with X-ray reflectivity. *Nano letters*, *16*(12), 7394-7401.
50. Seidlhofer, B. K., Jerliu, B., Trapp, M., Hüger, E., Risse, S., Cubitt, R., ... & Ballauff, M. (2016). Lithiation of crystalline silicon as analyzed by operando neutron reflectivity. *ACS nano*, *10*(8), 7458-7466.
51. Chon, M. J., Sethuraman, V. A., McCormick, A., Srinivasan, V., & Guduru, P. R. (2011). Real-time measurement of stress and damage evolution during initial lithiation of crystalline silicon. *Physical review letters*, *107*(4), 045503.
52. Zhang, S. (2017). Chemomechanical modeling of lithiation-induced failure in high-volume-change electrode materials for lithium ion batteries. *npj Computational Materials*, *3*(1), 1-11.
53. Grantab, R., & Shenoy, V. B. (2012). Pressure-gradient dependent diffusion and crack propagation in lithiated silicon nanowires. *Journal of the Electrochemical Society*, *159*(5), A584.
54. Sheldon, B. W., Soni, S. K., Xiao, X., & Qi, Y. (2011). Stress contributions to solution thermodynamics in Li-Si alloys. *Electrochemical and Solid-State Letters*, *15*(1), A9.
55. Liu, X. H.; Zhong, L.; Huang, S.; Mao, S. X.; Zhu, T.; Huang, J. Y. Size-Dependent Fracture of Silicon Nanoparticles during Lithiation. ACS Nano 2012, 6 (2), 1522–1531.
56. Cho, G. B., Noh, J. P., Sung, H. J., Lee, S. H., Im, Y. M., Ahn, H. J., & Kim, K. W. (2012). Patterned Si thin film electrodes for enhancing structural stability. *Nanoscale research letters*, *7*(1), 1-5.
57. Soni, S. K., Sheldon, B. W., Xiao, X., & Tokranov, A. (2011). Thickness effects on the lithiation of amorphous silicon thin films. *Scripta Materialia*, *64*(4), 307-310.
58. Xiao, X., Liu, P., Verbrugge, M. W., Haftbaradaran, H., & Gao, H. (2011). Improved cycling stability of silicon thin film electrodes through patterning for high energy density lithium batteries. *Journal of Power Sources*, *196*(3), 1409-1416.
59. Soni, S. K., Sheldon, B. W., Xiao, X., Verbrugge, M. W., Dongjoon, A., Haftbaradaran, H., & Huajian, G. (2011). Stress mitigation during the lithiation of patterned amorphous Si islands. *Journal of the Electrochemical Society*, *159*(1), A38.
60. Xu, R., & Zhao, K. (2016). Electrochemomechanics of electrodes in Li-ion batteries: A review. *Journal of Electrochemical Energy Conversion and Storage*, *13*(3).
61. Liu, M. (2015). Finite element analysis of lithiation-induced decohesion of a silicon thin film adhesively bonded to a rigid substrate under potentiostatic operation. *International Journal of Solids and Structures*, *67*, 263-271.
62. Bhandakkar, T. K., & Gao, H. (2010). Cohesive modeling of crack nucleation under diffusion induced stresses in a thin strip: Implications on the critical size for flaw tolerant battery electrodes. *International Journal of Solids and Structures*, *47*(10), 1424-1434.
63. Li, Y., Zhang, J., Zhang, K., Zheng, B., & Yang, F. (2019). A defect-based viscoplastic model for large-deformed thin film electrode of lithium-ion battery. *International Journal of Plasticity*, *115*, 293-306.
64. Everall, N. J. (2009). Confocal Raman microscopy: performance, pitfalls, and best practice. *Applied spectroscopy*, *63*(9), 245A-262A.
65. Poltorak, L., Dossot, M., Herzog, G., & Walcarius, A. (2014). Interfacial processes studied by coupling electrochemistry at the polarised liquid–liquid interface with in situ confocal Raman spectroscopy. *Physical Chemistry Chemical Physics*, *16*(48), 26955-26962.
66. Klassen, B., Aroca, R., & Nazri, G. A. (1996). Lithium perchlorate: Ab initio study of the structural and spectral changes associated with ion pairing. *The Journal of Physical Chemistry*, *100*(22), 9334-9338.
67. Plyushcheva, S. V., Mikhailov, G. M., Shabel'nikov, L. G., & Shapoval, S. Y. (2009). Tungsten thin-film deposition on a silicon wafer: The formation of silicides at W-Si interface. *Inorganic Materials*, *45*(2), 140-144.
68. Siegal, M. P., Graham, W. R., & Santiago, J. J. (1989). The formation of thin-film tungsten silicide annealed in ultrahigh vacuum. *Journal of applied physics*, *66*(12), 6073-6076.

69. Zheng, M., Tang, H., Hu, Q., Zheng, S., Li, L., Xu, J., & Pang, H. (2018). Tungsten-based materials for lithium-ion batteries. *Advanced Functional Materials*, *28*(20), 1707500.
70. Kim, J. J., Zhou, C., Mane, A. U., Suh, H. S., Kim, S., Shi, B., ... & Fister, T. T. (2022). Structural Changes during the Conversion Reaction of Tungsten Oxide Electrodes with Tailored, Mesoscale Porosity. *ACS nano*, *16*(4), 5384-5392.
71. He, Y., Yu, X., Li, G., Wang, R., Li, H., Wang, Y., ... & Huang, X. (2012). Shape evolution of patterned amorphous and polycrystalline silicon microarray thin film electrodes caused by lithium insertion and extraction. *Journal of Power Sources*, *216*, 131-138.
72. Han, F., Zhu, Y., He, X., Mo, Y., & Wang, C. (2016). Electrochemical stability of Li10GeP2S12 and Li7La3Zr2O12 solid electrolytes. *Advanced Energy Materials*, *6*(8), 1501590.
73. Zhu, Y., He, X., & Mo, Y. (2015). Origin of outstanding stability in the lithium solid electrolyte materials: insights from thermodynamic analyses based on first-principles calculations. *ACS applied materials & interfaces*, *7*(42), 23685-23693.
74. Thompson, T., Yu, S., Williams, L., Schmidt, R. D., Garcia-Mendez, R., Wolfenstine, J., ... & Sakamoto, J. (2017). Electrochemical window of the Li-ion solid electrolyte Li7La3Zr2O12. *ACS Energy Letters*, *2*(2), 462-468.
75. Wu, B., Wang, S., Lochala, J., Desrochers, D., Liu, B., Zhang, W., ... & Xiao, J. (2018). The role of the solid electrolyte interphase layer in preventing Li dendrite growth in solid-state batteries. *Energy & Environmental Science*, *11*(7), 1803-1810.
76. Han, F., Westover, A. S., Yue, J., Fan, X., Wang, F., Chi, M., ... & Wang, C. (2019). High electronic conductivity as the origin of lithium dendrite formation within solid electrolytes. *Nature Energy*, *4*(3), 187-196.
77. Pervez, S. A., Cambaz, M. A., Thangadurai, V., & Fichtner, M. (2019). Interface in solid-state lithium battery: challenges, progress, and outlook. *ACS applied materials & interfaces*, *11*(25), 22029-22050.
78. Lou, S., Zhang, F., Fu, C., Chen, M., Ma, Y., Yin, G., & Wang, J. (2021). Interface issues and challenges in all-solid-state batteries: lithium, sodium, and beyond. *Advanced Materials*, *33*(6), 2000721.
79. Lewis, J. A., Tippens, J., Cortes, F. J. Q., & McDowell, M. T. (2019). Chemo-mechanical challenges in solid-state batteries. *Trends in Chemistry*, *1*(9), 845-857.
80. Banerjee, A., Wang, X., Fang, C., Wu, E. A., & Meng, Y. S. (2020). Interfaces and interphases in all-solid-state batteries with inorganic solid electrolytes. *Chemical reviews*, *120*(14), 6878-6933.
81. Kerman, K., Luntz, A., Viswanathan, V., Chiang, Y. M., & Chen, Z. (2017). practical challenges hindering the development of solid state Li ion batteries. *Journal of The Electrochemical Society*, *164*(7), A1731.
82. Wang, Z., Santhanagopalan, D., Zhang, W., Wang, F., Xin, H. L., He, K., ... & Meng, Y. S. (2016). In situ STEM-EELS observation of nanoscale interfacial phenomena in all-solid-state batteries. *Nano letters*, *16*(6), 3760-3767.
83. Lou, S., Yu, Z., Liu, Q., Wang, H., Chen, M., & Wang, J. (2020). Multi-scale imaging of solid-state battery interfaces: from atomic scale to macroscopic scale. *Chem*, *6*(9), 2199-2218.
84. Le Van-Jodin, L., Ducroquet, F., Sabary, F., & Chevalier, I. (2013). Dielectric properties, conductivity and Li+ ion motion in LiPON thin films. *Solid State Ionics*, *253*, 151-156.
85. Srinivasan, E., & Parsons, G. N. (1995, September). Electronic properties of PECVD hydrogenated amorphous silicon with predominantly monohydride bonding deposited at less than 150/spl deg/C. In *Proceedings of Second International Workshop on Active Matrix Liquid Crystal Displays* (pp. 20-23). IEEE.
86. Huang, X. D., Zhang, F., Gan, X. F., Huang, Q. A., Yang, J. Z., Lai, P. T., & Tang, W. M. (2018). Electrochemical characteristics of amorphous silicon carbide film as a lithium-ion battery anode. *RSC advances*, *8*(10), 5189-5196.
87. Xu, Y., Yin, G., Ma, Y., Zuo, P., & Cheng, X. (2010). Nanosized core/shell silicon@ carbon anode material for lithium ion batteries with polyvinylidene fluoride as carbon source. *Journal of Materials Chemistry*, *20*(16), 3216-3220.
88. Adar, F., Lee, E., Mamedov, S., & Whitley, A. (2010). Experimental evaluation of the depth resolution of a Raman microscope. Microscopy and Microanalysis, 16(S2), 360-361.

89. Gruber, T., Thomas, D., Röder, C., Mertens, F., & Kortus, J. (2013). Raman spectroscopic studies of LixSiy compounds. *Journal of Raman Spectroscopy*, *44*(6), 934-938.
90. Stearns, L. A., Gryko, J., Diefenbacher, J., Ramachandran, G. K., & McMillan, P. F. (2003). Lithium monosilicide (LiSi), a low-dimensional silicon-based material prepared by high pressure synthesis: NMR and vibrational spectroscopy and electrical properties characterization. *Journal of Solid State Chemistry*, *173*(1), 251-258.